Chapter 11

Electrical Properties of Amorphous/Crystalline-Semiconductor Heterojunctions

Hideharu Matsuura and Hideyo Okushi

Electrochemical Laboratory, Tsukuba, Ibaraki, Japan

Single-crystalline heterojunctions have been studied extensively [1–7] over the years, and their applications to devices such as *heterojunction bipolar transistors* (HBT) with wide band-gap emitters [8], majority carrier rectifiers [2], beam-of-light transistors [9], indirect gap injection lasers [10], and solar cells [11] are well known. More recently, amorphous heterojunctions have also been used for some of these applications, which are described in this book.

Grigorovici [12] was the first to report the properties of amorphous/crystalline germanium heterojunctions. Stourac [13] later reported that the chalcogenide/crystalline-semiconductor heterojunction could be essentially approximated by the abrupt heterojunction and that the current transport mechanism could be based on the *space-charge-limited currents* (SCLC) in the amorphous materials. However, those materials were not appropriate for any device applications.

Since the first substitutional doping of the hydrogenated amorphous silicon (a-Si:H), achieved by Spear and LeComber [14] using the glow-discharge decomposition of SiH_4 mixed with either PH_3 or B_2H_6, a-Si:H has been a highly important material for device applications such as solar cells and thin-film transistors. The *current-voltage* (*I-V*) characteristics and *capacitance-voltage* (*C-V*) characteristics of undoped (and slightly *n*-type doped) a-Si:H/*p*-type crystalline-silicon (*p* c-Si) heterojunctions were reported in 1982 by Matsuura [15, 16]. Since that time the properties of a-Si:H/crystalline heterojunctions have been studied experimentally as well as theoretically [17–28]. Moreover, the applicability of a-Si:H/c-Si heterojunctions to devices such as vidicon targets of image pickup tubes [29, 30], gamma (γ)-ray detectors [31], solar cells [32–34], and HBT [35–47] has been investigated. The heterojunction has also been used to determine the energy distribution [$g(E)$]

of localized states in the gap for highly resistive amorphous semiconductors, such as undoped a-Si:H, hydrogenated amorphous silicon carbon alloy (a-$Si_{1-x}C_x$:H), and hydrogenated amorphous silicon germanium alloys (a-$Si_{1-x}Ge_x$:H) [48–51].

The main discussion in this chapter concerns a-Si:H/c-Si heterojunctions where the a-Si:H films were deposited by *glow discharge* (GD). We focus on the heterojunction electronic properties and relate these properties to the properties of amorphous semiconductors. At first, properties of contacts (ohmic or rectifying) between a-Si:H and c-Si are discussed. The *C-V* characteristics of the heterojunctions are discussed later on, and the method for determining $g(E)$ is proposed. Properties of *I-V* characteristics are also discussed. Finally, applications of a-Si:H/c-Si heterojunctions to different devices are summarized.

11.1 PROPERTIES OF CONTACTS BETWEEN AMORPHOUS SEMICONDUCTORS AND OTHER MATERIALS

Properties of contacts between a-Si:H and c-Si have been investigated by many authors [15–28]. In this section, we describe properties of diodes with the following four structures [52]: Type-1, (Au/a-Si:H/n^+-c-Si); Type-2, (Au/a-Si:H/p^+-c-Si); Type 3, (Mg/a-Si:H/n^+-c-Si); and Type 4, (Mg/a-Si:H/p^+-c-Si).

First we will describe the procedure by which these diode structures were fabricated. Crystalline Si wafers were first soaked in an HF solution to remove the SiO_2, then rinsed in distilled water. P-doped, B-doped, and undoped a-Si:H films, ~1.5 μm thick, were deposited at substrate temperature of 300°C on both n^+- and p^+-c-Si by means of glow-discharge decomposition of PH_3/SiH_4 or B_2H_6/SiH_4 gas mixtures. After the films' deposition, Au and Mg metals were evaporated onto the top surface of each a-Si:H film.

In the case of undoped a-Si:H shown in Figure 11.1(a), the Type-3 diode shows ohmic behavior and the current is limited by the bulk resistance of the a-Si:H film, which means that both contacts Mg/a-Si:H and n^+-c-Si/a-Si:H are ohmic. Currents of Type-2 and Type-4 diodes, for a positive bias on each metal, are of the same order of magnitude, indicating that these currents are limited by the reverse-biased p^+-c-Si/a-Si:H heterojunction in both diodes. Likewise, similarity between the *I-V* characteristics of Type-1 and Type-2 diodes for a negative-bias on Au implies that the currents are limited by the reverse-biased Au/a-Si:H Schottky barrier junction. The properties of the junctions involved in each diode with undoped films can then be classified qualitatively into "R" (rectifying) or "O" (ohmic), as is summarized in the first row of Table 11.1. The contact properties of undoped and P-doped a-Si:H are similar [53]; therefore, the undoped a-Si:H is thought to be intrinsically n-type. Undoped and P-doped a-$Si_{1-x}Ge_x$:H ($0 \leq x \leq 0.8$) also exhibit contact properties similar to that of a-Si:H [54], indicating that the undoped a-$Si_{1-x}Ge_x$:H is also intrinsically n-type.

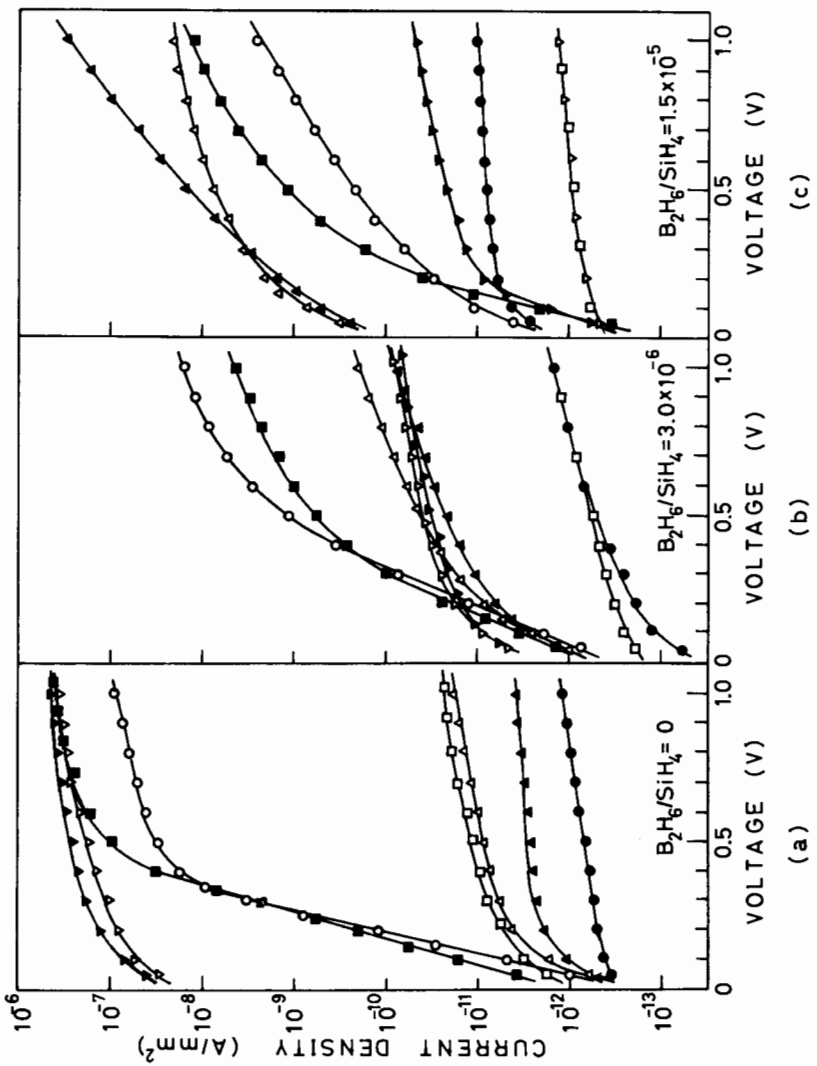

Figure 11.1 Current-voltage characteristics of four different types of diodes: ○, ●: Type 1 (Au/aSi:H/n⁺-c-Si); △, ▲: Type 2 (Au/a-Si:H/p⁺ c-Si); ▽, ▼: Type 3 (Mg/a-Si:H/n⁺-c-Si); and □, ■: Type 4 (Mg/a-Si:H/p⁺-c-Si). Open and solid marks represent data points for positive and negative bias voltage on metal, respectively. From: [52].

Table 11.1
Properties of Contacts With a-Si:H

a-Si:H	*Au*	*p^+ c-Si*	*Mg*	*n^+ c-Si*	*Conduction type**
P-doped and undoped	R	R	O	O	*n*
B_2H_6/SiH_4 10^{-6}	R	R	R	R	Intrinsic
B_2H_6/SiH_4 10^{-5}	O	O	R	R	*p*

R: rectification; O: ohmic
*Based on "dominant current concentration"

Diodes of B-doped a-Si:H with B_2H_6/SiH_4 ratios of 7.0×10^{-7}, 1.5×10^{-6}, and 3.0×10^{-6} exhibit *I-V* characteristics similar to each other, as shown in Figure 11.1(b). The forward currents of Type-1 and Type-4 diodes at higher voltages are limited by the resistance of the B-doped a-Si:H film. Since the forward currents of Type-2 and Type-3 diodes are substantially lower than the forward currents of Type-1 and Type-4 diodes at higher voltages, it is reasonable to consider Type-2 and Type-3 diodes as back-to-back diodes. Therefore, all junctions are rectifying type, as shown in Table 11.1. The slightly B-doped with $B_2H_6/SiH_4 \approx 10^{-6}$ a-Si:H is intrinsic in nature.

The analysis of the *I-V* characteristics for B-doped a-Si:H ($B_2H_6/SiH_4 = 1.5 \times 10^{-5}$, shown in Figure 11.1(c)) indicated that both O- and R-type junctions can be achieved. The results are summarized in Table 11.1. These results also indicate that film B-doped with $B_2H_6/SiH_4 > 10^{-5}$ is *p*-type.

11.2 CAPACITANCE-VOLTAGE CHARACTERISTICS OF AMORPHOUS/CRYSTALLINE HETEROJUNCTIONS

11.2.1 Energy-Band Diagram

Let us consider an undoped (slightly *n*-type) amorphous/*p*-type crystalline-silicon (*n*-a-Si:H/*p*-c-Si) heterojunction. Figure 11.2 shows an energy-band diagram, a potential $[u(x)/q]$ variation for electrons, and space charges produced by dc reverse bias (V) for such a heterojunction. When V is applied across the heterojunction, the depletion regions in both a-Si:H and c-Si are formed as shown in Figure 11.2(a). Because a-Si:H has continuous distribution of the gap states, the spatial distribution of the space charge in the a-Si:H depletion region is not simple. The differences between the a-Si:H depletion region ($0 \leq x \leq W_2$) and the neutral region ($x > W_2$) are based on:

1. Whether electrons exist at gap states below the Fermi level (E_F);
2. Whether electrons exist in the conduction band as well as in the conduction bandtail.

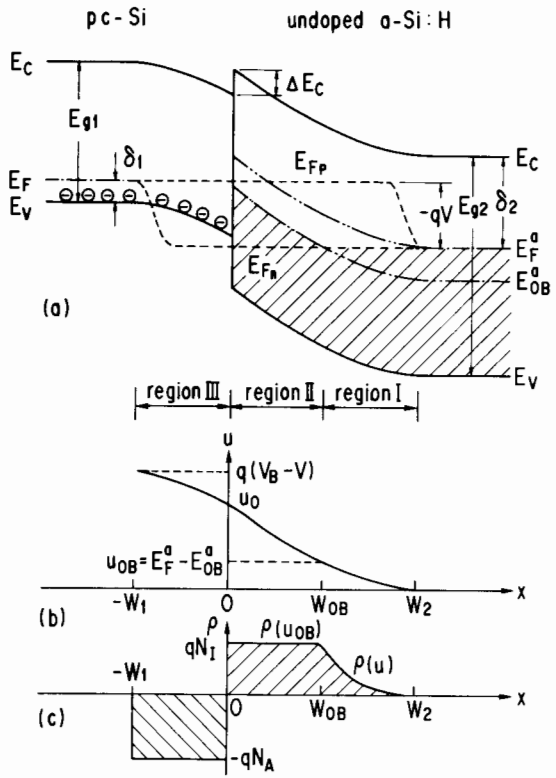

Figure 11.2 Schematic sketches of heterojunction: (a) energy-band diagram, (b) potential variation for electron, and (c) space-charge density variation for reverse-bias voltage condition. Localized states indicated by hatched area of (a) are occupied by electron.

These changes will result in the formation of space charge in the depletion region of a-Si:H. In this analysis, therefore, charged states (e.g., shallow donors) in the neutral and depletion regions need not be explicitly considered.

The occupation of the gap states in the depletion region is governed by a balance between the thermal emissions of electrons and holes and the capture processes of electrons and holes at the gap states [56, 57]. It is useful, therefore, to consider the quasi-Fermi levels of electrons (E_{Fn}) and holes (E_{Fp}) in the depletion region, and one particular energy level (E_{OB}) for which the thermal-emission rate for electrons equals that for holes. E_{Fn} is almost constant in the whole depletion region and rises toward the Fermi level near the edge of the depletion region of *p*-c-Si, while E_{Fp} falls near the edge of the depletion region of a-Si:H, as shown in Figure 11.2(a). On the other hand, E_{OB} of a-Si:H is given by [49, 57, 58]:

$$E_{OB} = E_V + E_{g2}/2 + (kT/2)\ln(\nu_p/\nu_n) \tag{11.1}$$

Here, E_V is the top of the valence band of a-Si:H, E_{g2} is the energy bandgap of a-Si:H and ν_n and ν_p are the pre-exponential factors of thermal-emission rates (attempt-to-escape frequencies) for electrons and holes at the gap states, respectively.

Now we consider the space charge in the two depletion regions (region I and region II) of a-Si:H divided by the cross point (W_{OB}) at $E_{Fn} = E_{OB}$. In region I ($W_{OB} < x \leq W_2$), where E_{Fn} is above E_{OB}, the space-charge density (ρ) at the spatial position (x) is expressed as

$$\rho[u(x)] = \int_{E_F^a - u(x)}^{E_F^a} g(E)\, \mathrm{dE} \tag{11.2}$$

where $u(x)$ is the potential energy shown in Figure 11.2(b), E_F^a is the Fermi level at the neutral region, and $g(E)$ the density-of-state distribution in a-Si:H. Here, for simplicity, the Fermi-Dirac distribution function and the electron occupation of the gap states are approximated by the step functions.

In region II ($0 \leq x \leq W_{OB}$), where E_{Fn} is below E_{OB}, the space-charge density is kept constant and is expressed as

$$\rho(u_{OB}) = \int_{E_F^a - u(x)}^{E_F^a} g(E)\, dE \tag{11.3}$$

and

$$qN_I = \rho(u_{OB}) \tag{11.4}$$

with

$$u_{OB} = E_F^a - E_{OB}^a \tag{11.5}$$

where u_{OB} is the potential energy at W_{OB}, N_I the density of midgap states between E_F^a and E_{OB}^a in the a-Si:H, and E_{OB}^a is E_{OB} in the neutral region of a-Si:H. At thermal equilibrium (i.e., $V = 0$V), when the built-in potential for a-Si:H is larger than the value of $(E_F^a - E_{OB}^a)/q$, $\rho(x)$ near the interface exceeds qN_I because the Fermi level is below E_{OB} near the interface. This situation near the interface remains the same even when the reverse bias is applied. However, as will be discussed later, the contribution of the excess charges near the interface can be included in the effect of charged states in the near-interface region.

In the depletion region in p-c-Si, which is region III ($-W_1 \leq x < 0$) in Figure 11.2, the space-charge density is given by $-qN_A$ under assumption that the p-c-Si has only shallow acceptors whose density is N_A. As a consequence, the space-charge density can be schematically shown in Figure 11.2(c).

11.2.2 Simulation of High-Frequency Capacitance-Voltage Characteristics

Based on the energy-band diagram mentioned above, let us consider theoretically the C-V characteristics of the amorphous/crystalline heterojunctions. It should be pointed out that a great deal of C-V characteristics and modeling has been carried out [59–62] on a-Si:H Schottky barrier diodes. Simulations of C-V characteristics of the amorphous/crystalline heterojunctions at 0 Hz were also reported [21, 24–26], but it is experimentally difficult to measure the very low frequency C-V characteristics that will correspond to the simulation data. Moreover, C-V characteristics vary with the measuring frequency because of the dielectric relaxation and trapping/detrapping processes in the amorphous film.

On the other hand, it is easy to measure high-frequency (e.g., 1-MHz) C-V characteristics [63–66], and when the measuring frequency is high enough, the dielectric relaxation process, as well as the trapping/detrapping process, can be neglected in the amorphous film, so the change in width of the depletion region in the crystalline semiconductor, produced by the dc reverse bias, is only needed to calculate the capacitance. This leads to an accurate simulation of the high-frequency C-V experimental characteristics of amorphous/crystalline heterojunctions. The analytical approach here is that the contribution of a-Si:H to the measured capacitance is equal to the geometric capacitance of the a-Si:H film due to its longer dielectric relaxation time, whereas that of c-Si is associated with the depletion width of c-Si. The measured capacitance is essentially the result of two capacitances in series. In the following, we discuss the simulation conditions for high-frequency C-V characteristics of the amorphous/crystalline heterojunctions.

The potential $u(x)/q$ for electron can be derived from the Poisson equation

$$d^2[u(x)/q]/d^2x = \rho/\epsilon_{s2} \tag{11.6}$$

where ϵ_{s2} is the semiconductor permittivity for a-Si:H. The space-charge Q_I in region I ($W_{OB} < x \leq W_2$) is given by [67]

$$Q_I = [2\epsilon_{s2}\int_0^{u_{OB}} \rho(u)\, du]^{1/2} \tag{11.7}$$

and the electric field (E_I) at $x = W_{OB}$ is given by [67]

$$E_I = Q_I/\epsilon_{s2} \tag{11.8}$$

In region II, (11.7) can be solved easily with the boundary conditions of $u(0) = u_0$, $-du/dx|_{x=W_{OB}} = E_I$, and $u(W_{OB}) = u_{OB}$, because $\rho = qN_I$, where N_I is constant in the region. The value of W_{OB} is calculated as a function of u_0. Then, the width (W_1) of the depletion region in p-c-Si is estimated from the charge neutrality.

$$qN_AW_1 = qN_IW_{OB} + Q_1 \tag{11.9}$$

and the reverse voltage is calculated from the relation

$$V_B - V = u_0/q + (qN_AW_1^2)/2\epsilon_{s2} \tag{11.10}$$

where V_B is the built-in voltage and ϵ_{s1} is the semiconductor permittivity for c-Si.

Finally, the high-frequency capacitance (C) is estimated as

$$C = S(\epsilon_{s1}/W_1 + \epsilon_{s2}/L) \tag{11.11}$$

because of the long dielectric relaxation time (ϵ_{s2}/σ_2) of undoped a-Si:H, where L is the thickness of a-Si:H, σ_2 is the dark conductivity of a-Si:H, and S is the electrode area.

To calculate the N_I in (11.4) we need to know the density-of-state distribution $g(E)$ of a-Si:H. Because the main gap states in the a-Si:H are the dangling bonds, we assume $g(E)$ to have a gaussian distribution given by

$$g(E) = g_{max}\exp\{-[(E - E_p)^2/2E_W^2]\} \tag{11.12}$$

where g_{max} is the maximum value of the gaussian distribution, E_p is the energy level of the maximum value, and E_W is the half-width of the distribution.

Next we consider the interface states and the states located in the near-interface region that is qualitatively different from the bulk region. Here we assume one kind of positively charged layer having the thickness d_s and the density N_{SS}. This layer is located between p-c-Si and a-Si:H and represents the interface and near-interface regions of the heterojunction. This layer is called an interface layer in this chapter, and the charge Q_{ss} per unit area is given by $N_{ss}d_S$. If the effect of the interface layer cannot be neglected (11.10) becomes

$$\begin{aligned} qN_AW_1 &= qN_IW_{OB} + Q_I + Q_{ss} \\ &= qN_IW_{OB} + Q_I + N_{ss}d_s \end{aligned} \tag{11.13}$$

The parameters used in the present simulation are given in Table 11.2 and almost all of the parameters are fixed. The ϵ_{s1} is also assumed to be equal to ϵ_{s2}.

Table 11.2
Parameters Used for Simulating High-Frequency C-V Characteristics

Amorphous film			
Neutral region	*Midgap states*	*Interface layer*	*Others*
$E_C - E_F^a = 0.73$ eV	$E_C - E_P = 0.85$ eV	$N_s = 0$–10^{18} cm^{-3}	$V_B = 0.85$ eV
$E_C - E_{OB}^a = 0.97$ eV	$E_W = 0.10$ eV	$d_s = 0$ or 50Å	$L = 1.2$ μm
	$g_{max} = 1$ or 3×10^{16} cm^{-3} eV^{-1}		$S = 0.785$ mm^2
			$N_A = 10^{15}$, 10^{16} cm^{-3}

11.2.3 Steady-State Heterojunction-Monitored Capacitance Method

The steady-state *heterojunction-monitored capacitance* (HMC) method [15, 16, 49, 63] has been proposed to experimentally determine the midgap-state densities in amorphous semiconductors and the built-in voltages of the amorphous/crystalline heterojunction from the high-frequency C-V characteristics. In the HMC method, we neglect the region I shown in Figure 11.2 and the interface layer, and we adopt the depletion approximation for both depletion regions.

If we neglect region I shown in Figure 11.2, the depletion region charge-neutrality condition gives

$$qN_AW_1 \cong qN_IW_{OB} \tag{11.14}$$

Using the Poisson equation, relationship between reverse voltage and depletion width p-c-Si is given by

$$V_B - V - u_0/q = qN_AW_1^2/2 \Rightarrow 2\epsilon_{s1} \tag{11.15}$$

For a-Si:H we can obtain

$$u_0/q = qN_IW_{OB}^2/2 \Rightarrow 2\epsilon_{s2} \tag{11.16}$$

where u_0/q is the potential at $x = 0$ as shown in Figure 11.2.

From (11.15) and (11.16),

$$V_B - V = qN_AW_1^2/2\epsilon_{s1} + qN_IW_{OB}^2/2\epsilon_{s2} \tag{11.17}$$

and from (11.14), (11.17) is rewritten as

$$V_B - V = W_1^2/N_I(qN_AN_I/2\epsilon_{s1} + qN_A^2/2\epsilon_{s2}) \tag{11.18}$$

Then, we obtain

$$W_1^2 = 2\epsilon_{s1}\epsilon_{s2}N_I(V_B - V)/qN_A(N_I\epsilon_{s2} + qN_A\epsilon_{s1}) \tag{11.19}$$

Since the high-frequency capacitance (C) is given by (11.11), W_1^2 is given by

$$W_1^2 = [\epsilon_{s1}(1/C - 1/C_2)]^2 \tag{11.20}$$

where C is the capacitance of the amorphous film measured at a frequency higher than $\sigma_2/2\pi\epsilon_{s2}$ and C_2 is the saturated capacitance obtained at higher forward bias which is given by ϵ_{s2}/L.

In the HMC method, the W_1^2–V relation is obtained from the C–V characteristics using (11.14), then N_I and V_B are graphically estimated using (11.19). However, as mentioned above, (11.19) is derived by neglecting the region I and interface layers. Therefore, N_I and V_B, graphically estimated by using (11.19), are slightly different from the real values of N_I and V_B. We denote hereafter the midgap-state densities and the built-in voltages estimated by the HMC method as $^*N_I$ and $^*V_B$. In the following section, we compare $^*N_I$ and $^*V_B$ with the real values of N_I and V_B.

11.2.4 Reliability of HMC Method

Figure 11.3(a) shows the simulated high-frequency C-V characteristics of an amorphous/crystalline heterojunction (with parameters of $g_{max} = 10^{16}$ cm^{-3} eV^{-1} and $N_A = 10^{15}$ cm^{-3}), and Figure 11.3(b) shows the $W_1^2 - V$ relation obtained from the C-V curve given in Figure 11.3(a) by using (11.20). According to (11.19), $^*N_I$ and $^*V_B$ can be graphically obtained from the slope and the intercept on the abscissa, respectively. The $^*N_I$ value obtained in the reverse-bias region ($-6\text{V} \le V \le -1\text{V}$) is 2.5×10^{15} cm^{-3}. This value is close to $N_I = 2.0 \times 10^{15}$ cm^{-3} calculated from (11.3) and (11.4) using the parameters given in Table 11.2 ($g_{max} = 10^{16}$ cm^{-3} eV^{-1}). The value of $^*V_B$, which is obtained from the intercept of the straight line drawn in the reverse-bias region ($-6\text{V} \le V \le -1\text{V}$) on the abscissa, is 0.21V. This value is a little lower than the calculated value of $V_B = 0.30$V, because the additional potential u_{OB}/q is necessary to make the space-charge density constant.

The simulated high-frequency C-V characteristics were similar to Figure 11.3, in which the interface layer was taken into account, although the lowest reverse bias, where the discrepancy from the straight line starts to occur, is higher than

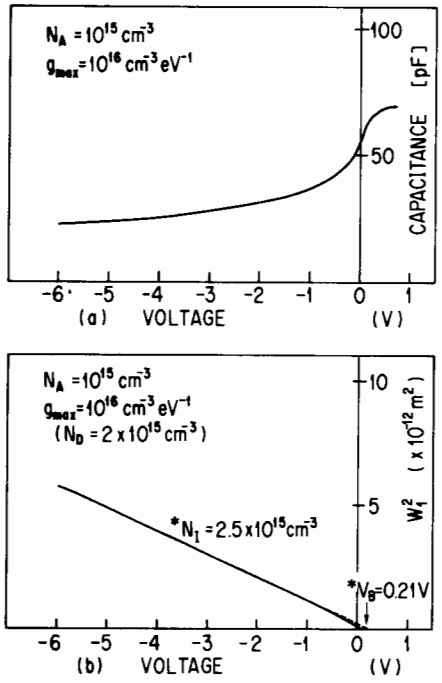

Figure 11.3 Shown are (a) calculated capacitance-voltage characteristics and (b) voltage dependence of square of depletion width in crystalline semiconductor. The $^*N_I$ and $^*V_B$ values given are obtained from steady-state HMC methods. Solid line is calculated data, and dashed line is line extrapolated from high reverse biases (interface neglected).

the reverse bias (about 0.7V) calculated without the effect of the interface layer. Figure 11.4 shows the dependence of $^*N_I$ and $^*V_B$ on the charge ($Q_{ss} = N_{ss}d_s$) for $g_{max} = 3 \times 10^{16}$ cm^{-3} eV^{-1} and $N_A = 10^{16}$ cm^{-3}. In the range of $N_{ss} \le 2 \times 10^{17}$ cm^{-3}, the values of $^*N_I$ and $^*V_B$ are quite close to N_I and V_B, respectively, then they increase rapidly with N_s. These increases result from Q_{ss}.

It is clear from the above results that if Q_{ss} is low, $^*N_I$ and $^*V_B$ obtained by the HMC method represent the real midgap-state density and the real built-in voltage, respectively. The Q_{ss} value is important for discussing the reliability of the result obtained by the HMC method, but the experimental determination of Q_{ss} is quite difficult. Therefore, it is judged experimentally from the value of $^*V_B$, as is clearly shown in Figure 11.4, whether $^*N_I$ is close to the real midgap-state density or not. For example, if $^*V_B$, obtained by the HMC method, is close to V_B value estimated from I-V characteristics (Section 11.4.2) $^*N_I$ is close to the real midgap-state density.

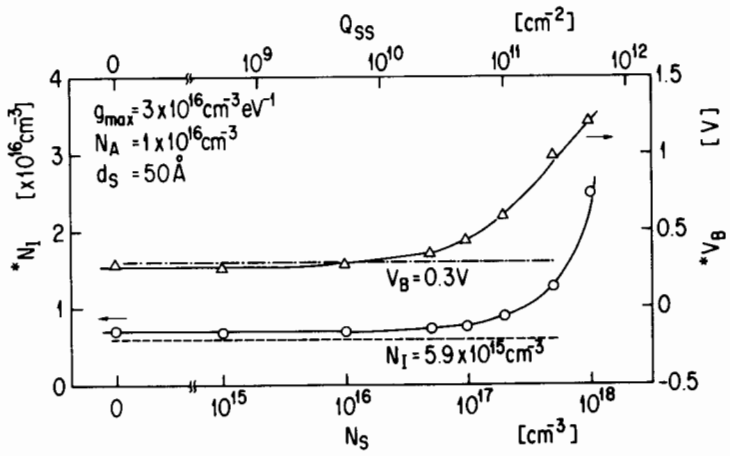

Figure 11.4 Dependences of $*N_I$ and $*V_B$ values on density of interface layer.

11.2.5 Experimental Capacitance-Voltage Characteristics

Figure 11.5 shows typical high-frequency (1-MHz) *C-V* characteristics of the undoped a-Si:H/*p* c-Si ($N_A = 10^{16}$ cm^{-3}) heterojunction. When *p*-c-Si is replaced by p^+-c-Si, having the resistivity of less than 0.01 Ωcm, the capacitance was found to be independent of applied voltage. The value of this capacitance is determined by the film thickness of undoped a-Si:H layer. In undoped a-Si:H the thermal-emission rates of electrons from the localized states to the conduction band are usually much lower than the capture rates of electrons from the conduction band into the localized states, therefore, the capacitance should be measured from a higher to a lower reverse bias. Moreover, the voltage sweep rate (dV/dt) should be small, for example, the dV/dt should be smaller than 0.004 V/s, and the heterojunction at higher reverse bias (starting bias for the *C-V* measurements) should be kept for a few minutes in order to get the steady-state condition. To explain the *C-V* characteristics two models have been proposed:

1. A *metal-oxide-semiconductor* (MOS)-type model [64, 65], where a-Si:H is considered to behave as an oxide layer;
2. A *p-n* junction-type model, mentioned above [16].

In the MOS-type analysis, the quasi-Fermi level for electrons is assumed to coincide with the quasi-Fermi level for holes in the depletion region, which means that at any applied voltage the Fermi level can be defined in the depletion region. Therefore, this type of analysis could only be applied to a heterojunction across which the current does not flow. In the *p-n* junction-type analysis, when a voltage is applied across the junction, the quasi-Fermi level for electrons is separated from

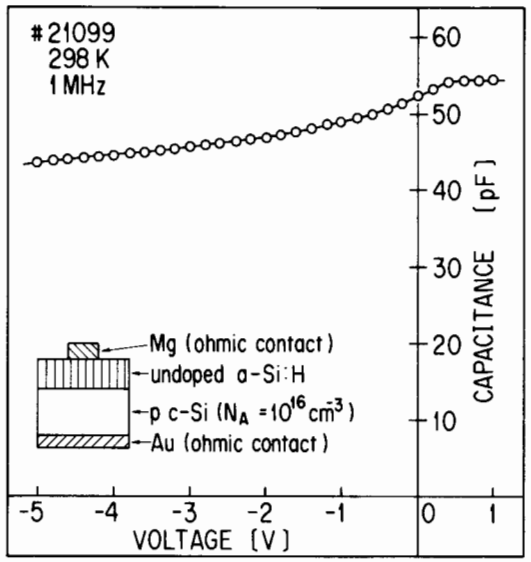

Figure 11.5 Room temperature capacitance-voltage characteristics of undoped a-Si:H/*p*-c-Si ($N_A = 10^{16}$ cm^{-3}) heterojunction. From: [88].

the quasi-Fermi level for holes in the depletion region. Therefore, the *p-n* junction-type analysis should be applied to a heterojunction across which the current does flow. The a-Si:H/c-Si heterojunction behaves as a *p-n* heterojunction (Section 11.4); therefore, the *C-V* characteristics should be analyzed by using the *p-n* junction-type analysis.

Figure 11.6 shows the temperature dependence of the *C-V* characteristics for the a-Si$_{1-x}$Ge$_x$:H/*p*-c-Si heterojunction. The value of $\sigma_2/2\pi\epsilon_{s2}$ corresponding to 304K remains lower than 1 MHz. The frequency dependence of the *C-V* characteristics for the a-Si:H/*p*-c-Si heterojunction at 298K is shown in Figure 11.7. The frequency of 1 kHz remains higher than $\sigma_2/2\pi\epsilon_{s2}$ (about 150 Hz). The *C-V* characteristics measured at 100 Hz were much different from those given in Figure 11.7. The saturated capacitance observed at high forward bias for 1-MHz curve did not appear at lower frequencies because the capacitance in the a-Si:H is no longer determined by the thickness of the a-Si:H film. In both figures, the capacitance measured at $V > -2$V depends on the temperature and frequency. However, the capacitance measured at $V < -2$V is temperature and frequency-independent (in this region of the *C-V* curve the capacitance is higher than $\sigma_2/2\pi\epsilon_{s2}$), indicating that N_I values are reliable if it is obtained in the high reverse-bias region of the *C-V* curve.

Figure 11.8 shows the $W_i^2 - V$ relationship obtained from Figure 11.5. A good linear relationship shown in this figure indicates that the *p-n* junction-type

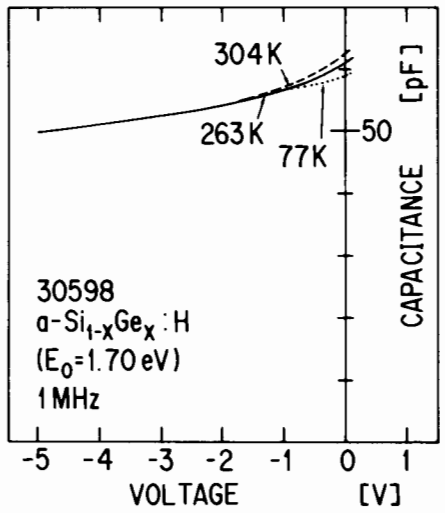

Figure 11.6 The influence of the temperature on 1-MHz *C-V* curves for the undoped a-$Si_{1-x}Ge_x$:H (E_0 = 1.70 eV)/*p*-c-Si (N_A = 10^{16} cm^{-3}) heterojunction. From: [47].

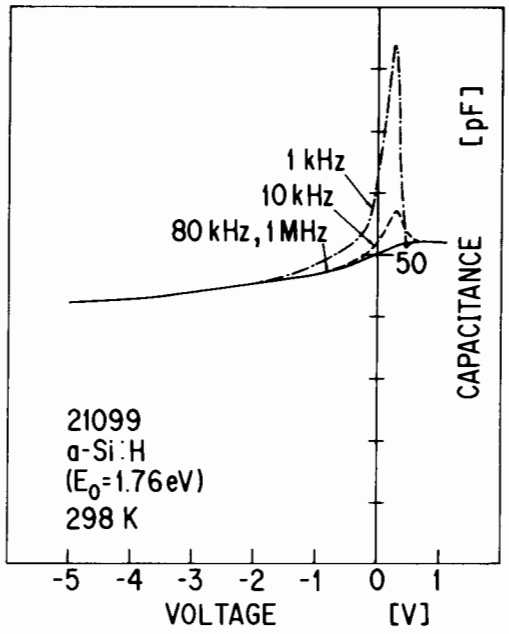

Figure 11.7 Influence of frequency on 298K *C-V* characteristics for undoped a-Si:H/*p*-c-Si (N_A = 10^{16} cm^{-3}) heterojunction. From: [47].

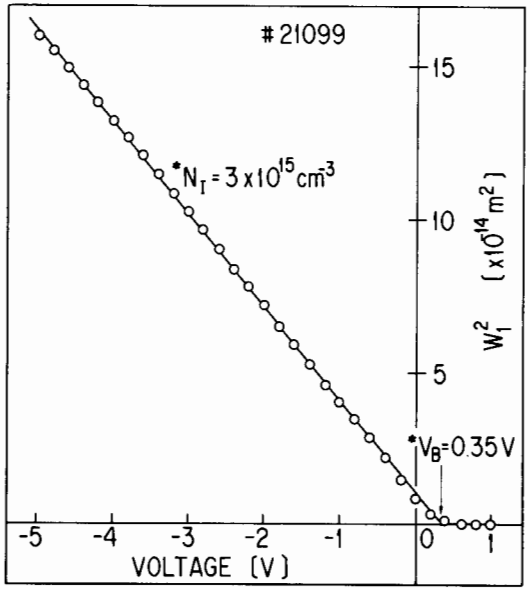

Figure 11.8 Variation of square of width of depletion region in *p*-c-Si as a function of bias voltage. From: [48].

analysis is applicable to the present system. Using (11.15), the N_I and V_B values can be determined from the slope and the intercept on the abscissa, respectively, as shown in Figure 11.8, where the N_I and V_B obtained are 3 × 10^{15} cm^{-3} and 0.35V, respectively.

Figure 11.9 shows the relationship between N_I and the optical gap (E_O), and the relationship between N_I and the bulk spin densities (N_s) obtained from the *electron-spin resonance* (ESR) measurements. It is clear from the insert (Figure 11.9) that the values of N_I and N_s are very similar. This correspondence could indicate that N_I represents the density of singly occupied dangling bonds (D^0) seen by ESR. It is noted here that the *p-n* junction-type analysis has also been reported to hold for B-doped a-Si:H/*n*-c-Si heterojunctions [18, 30].

11.2.6 The Band Discontinuity Between Amorphous and Crystalline Semiconductors

Knowing band discontinuities at the amorphous/crystalline-semiconductors heterojunctions is important in order to describe its electrical properties. Many studies of the band discontinuity have been reported over the past several years [15–18, 28, 67, 69–72]. In this section, we discuss the conduction-band discontinuity (ΔE_C)

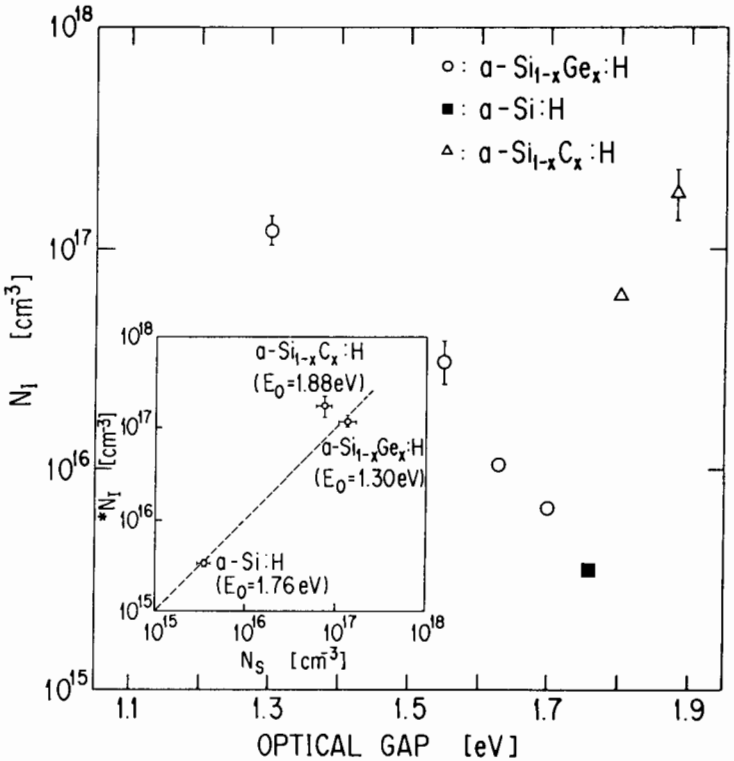

Figure 11.9 Densities of midgap states of undoped films having various optical band gaps. Relation between $*N_t$ and bulk spin density (N_s) obtained from ESR is also given in insert. From: [51].

at a-Si:H/*p*-c-Si heterojunctions based on experimental results mentioned in Section 11.2.4.

If we assume the energy-band diagram shown in Figure 11.2 (see Section 11.2.1), the conduction band continuity is expressed by

$$\Delta E_C = \delta_1 + \delta_2 - E_{g1} + qV_B \tag{11.21}$$

where $\delta_1 = E_F - E_V$ at *p*-c-Si substrate, $\delta_2 = E_C - E_F$ at a-Si:H, E_{g1} is the energy gap for *p*-c-Si, and V_B is the built-in voltage at the junction. Experimentally, δ_1 is estimated from N_A and δ_2 from the activation energy of dark conductivity of a-Si:H. Based on Figure 11.8 data, we find that $V_B = 0.35$V, then using (11.21) for $\delta_1 = 0.18$ eV, $\delta_2 = 0.73$ eV, and $E_{g1} = 1.12$ eV, the δE_C was estimated to be 0.14 eV. The average value for ΔE_C was 0.20 eV [16], indicating that the main

band discontinuity occurs in the valence band; $\Delta E_C + \Delta E_V = E_{g2} - E_{g1} = 1.76$ eV $- 1.12$ eV $= 0.64$ eV.

Similar results for a-Si:H/c-Si heterojunction were recently obtained by Mimura and Hatanaka using an internal photoemission technique [67], and by Essick and Cohen using novel junction capacitance technique [28]. The latter results indicate a nearly zero conduction band offset (50 ± 50 meV) and slightly larger valence band offset $\Delta E_V = 0.58 \pm 0.02$ eV. It should be noted that the determination of ΔE_C using (11.21) has some uncertainties. For example, the exact position of the Fermi energy in undoped a-Si:H, which corresponds to δ_2, is quite difficult to obtain because of the statistical shifts resulting from the Mayer-Nudel rule [69]. Recently, Sharma and Narasimhan have examined in detail the limitation of the HMC method [70]. They have concluded that from a measurement of the bias dependence of the high-frequency capacitance of a-Si:H/c-Si heterojunction, it is possible to obtain a good estimate of the total integrated number of the deep-gap states in a-Si:H, but the values of V_B obtained by this method are not reliable because of the interface effect and hence cannot be used to estimate exact band discontinuities [70].

The internal photoemission studies on the band discontinuity have also been applied in the cases of *sputtered* (SP) a-Si:H [71, 72] and *evaporated* (EV) amorphous silicon/c-Si heterojunctions [73]. In contrast with a glow-discharged a-Si:H, ΔE_V was reported to be close to zero in these cases. Based on these results, the ΔE_C and ΔE_V values depend strongly on the interface and bulk properties. Therefore, for the device applications it is important to know the quality of the interface and amorphous semiconductors used in amorphous/crystalline-semiconductor heterojunction.

11.3 TRANSIENT CAPACITANCE OF AMORPHOUS/CRYSTALLINE HETEROJUNCTION

11.3.1 Transient Capacitance

It is clear for the previous section that the measurement of $g(E)$ and an understanding of the nature of the gap states is very important to enhance the performance of a-Si:H-based devices. The problem has received considerable attention, and many techniques have been developed to determine $g(E)$, including optical and electrical methods. Transient capacitance methods like *deep-level transient spectroscopy* (DLTS) [74] and *isothermal capacitance transient spectroscopy* (ICTS) [75] are tested techniques for determination of $g(E)$ in a-Si:H; however, these methods are limited in their application to doped samples having low resistivities. For high-resistivity materials, dielectric relaxation times are too long for measurement of capacitance, which can reflect the depletion width of the a-Si:H junction. However, a capacitance transient of high-resistivity undoped a-Si:H/*p* c-Si heterojunctions

can be detected. Figure 11.10 shows the change in the capacitance at the zero-bias condition of the undoped a-Si:H/*p*-c-Si ($N_A = 10^{16}$ cm^{-3}) heterojunction after a reverse-bias voltage (−4V) is applied to the sample for a certain time. Because a-Si:H possesses deep-gap states whose emission rates are small, the capacitance gradually decreases with time. From the transient behavior of capacitance, the $g(E)$ in undoped a-Si:H can be defined.

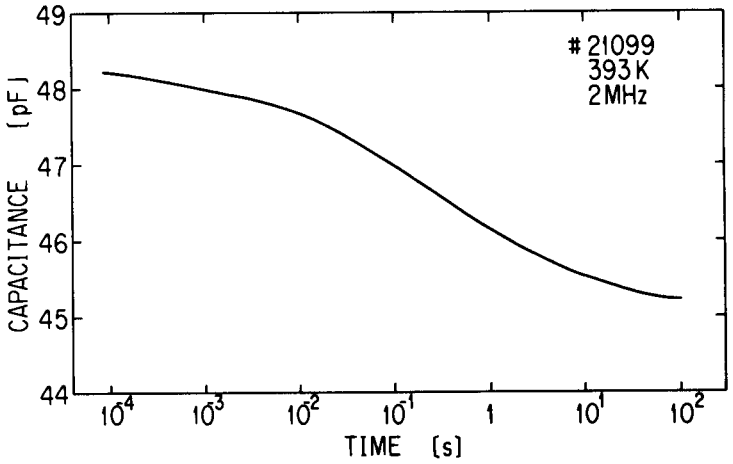

Figure 11.10 Transient capacitance of undoped a-Si:H/*p* c-Si ($N_A = 10^{16}$ cm^{-3}) heterojunction. From: [48].

Another method of measuring capacitance transient for high-resistivity films is a photocapacitance transient spectroscopy [76], which has been used recently by Gelatos and Kanicki to investigate the properties of the silicon nitrite/a-Si:H interface states [77].

11.3.2 Theory of Transient Heterojunction-Monitored Capacitance Method

This section discusses the method used to determine $g(E)$ below the Fermi level in undoped (highly resistive) amorphous films. In order to estimate $g(E)$, the transient HMC is considered after a reverse-bias voltage (V) is applied to the sample for a certain period of time, as shown in Figure 11.11. In the transient HMC method discussed here, we neglect region I, shown in Figure 11.2, and the interface layer. At $t = +0$ the voltage is applied across the heterojunction as shown in Figure 11.11(b). Electrons trapped at shallower states are thermally emitted into

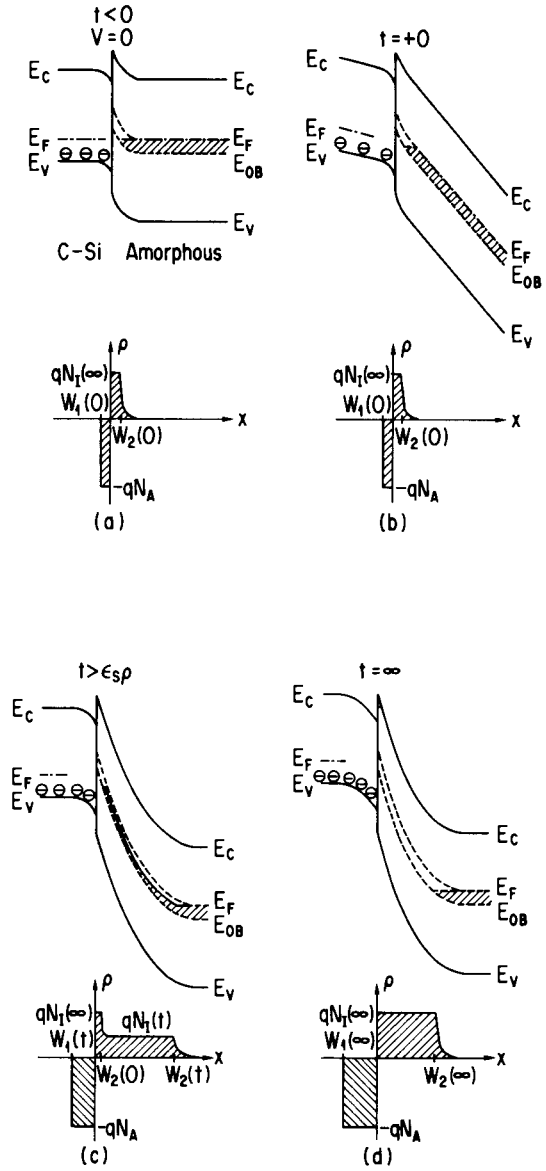

Figure 11.11 Schematic representation of energy-band diagram and space-charge density of heterojunction at four different times. In energy-band diagrams, localized states as indicated by hatched area are occupied by electrons, so are neutral. In depletion region, therefore, empty localized states between E_F and E_{OB} behave as positively charged states. States below E_{OB} are always occupied by electrons; ⊖ represents negatively charged acceptor.

the conduction band. For t larger than the dielectric relaxation time of the amorphous film, the space charge in the vicinity of the heterojunction will redistribute itself in response to the applied potential (Figure 11.11(c)).

The HMC data after dielectric relaxation can be analyzed using (11.15), where W_1 and N_I will be a function of time (t), thus

$$W_1^2(t) = 2\epsilon_{s1}\epsilon_{s2}N_I(t)(V_B - V)/qN_A[N_I(t)\epsilon_{s2} + qN_A\epsilon_{s1}] \tag{11.22}$$

If

$$V_C(t) = qN_AW_1^2(t)/2\epsilon_{s1} \tag{11.23}$$

(11.22) can be rewritten as

$$V_C(t)[N_I(t)\epsilon_{s2} + qN_A\epsilon_{s1}] = \epsilon_{s2}N_I(t)(V_B - V) \tag{11.24}$$

By solving $N_I(t)$ from (11.22), we obtain

$$N_I(t) = \epsilon_{s1}V_C(t)N_A/\epsilon_{s2}[V_B - V - V_C(t)] \tag{11.25}$$

From (11.11) we can also obtain

$$W_1(t) = \epsilon_{s1}[1/C(t) - 1/C_2] \tag{11.26}$$

where $W_1(t)$ is the depletion width in c-Si at time t and $V_C(t)$ is the voltage at t across the depletion region of c-Si. To make the above analysis feasible, the absolute value of V must be much higher than V_B, so that the $N_I(t)W_2(t) \gg N_I(0)W_2(0)$ and the average value of N_I over the depletion region at t is close to $N_I(t)$. This condition also suggests that interface states do not affect the measurement of HMC.

Now we consider the change in the space-charge density $\Delta N_I(t)$ defined by

$$\Delta N_I(t) \equiv N_I(t) - N_I(\infty) \tag{11.27}$$

$\Delta N_I(t)$ is determined by the change in the electron occupation of the density-of-state distribution $g(E)$ with an exponential decay corresponding to the thermal emission processes of electrons and holes, thus:

$$\Delta N_I(t) = \int_{E_V}^{E_C}[f(E) - F_\infty(E)]g(E)\exp\{-[e_n(E) + e_p(E)]t\}\,dE \tag{11.28}$$

where E_C (E_V) are the conduction (valence) band edge, $f(E)$ and $F_\infty(E)$ are the occupation functions at $t = 0$ and $t = \infty$, respectively, and $e_n(E)$ [$e_p(E)$] is the

thermal emission rate of electrons (holes). The function $f(E)$ corresponds to Fermi-Dirac distribution function

$$f(E) = 1/\{1 + \exp[(E - E_F)/kT]\} \tag{11.29}$$

and $F_\infty(E)$ is given by the thermal-emission process

$$F_\infty(E) = e_p(E)/[e_n(E) + e_p(E)] \tag{11.30}$$

The $e_n(E)$ and $e_p(E)$ are given by

$$e_n(E) = \nu_n \exp[(E - E_C)/kT] \tag{11.31}$$

and

$$e_p(E) = \nu_p \exp[(E_V - E)/kT] \tag{11.32}$$

Here, we defined the function $H(t)$ as

$$H(t) = \int t[\Delta N_I(t)/dt] \tag{11.33}$$

Then from (11.28) we obtain

$$H(t) = \int_{E_V}^{E_C}[f(E) - F_\infty(E)]g(E)\,[e_n(E) + e_p(E)]$$

$$t\exp\{-[e_n(E) + e_p(E)]t\}\,dE \tag{11.34}$$

$$= \int_{E_V}^{E_C}[f(E) - F_\infty(E)]g(E)]D(E, t)\,dE$$

where

$$D(E, t) = [e_n(E) + e_p(E)]t\exp\{-[e_n(E) + e_p(E)]t\} \tag{11.35}$$

The function $D(E, t)$ is maximum at $[e_n(E) + e_p(E)]t = 1$ and can be approximated using a delta function

$$D(E, t) = kT\,d(E - E_m) \tag{11.36}$$

where E_m is the energy at which $D(E, t)$ has a maximum value when $[e_n(E_m) + e_p(E_m)]t_m = 1$. If $e_n(E) \gg e_p(E)$ the relation between E_m and t_m is derived from (11.31):

$$E_C - E_m = kT \ln(\nu_m t_m) \tag{11.37a}$$

In a more general form, this equation can be expressed as

$$E_C - E(t) = kT \ln\{\nu[E(t)]t\} \tag{11.37b}$$

Under the condition that the emission rate (e_n) for electrons is much higher than that (e_p) for holes ($F_\infty(E) = 0$) and the Fermi-Dirac distribution function $f(E)$ is close to unity (for the gap states between E_F^a and E_{OB}^a, we can obtain the relationship between $H(t)$ and $g(E)$ from (11.34) to (11.36) and by assuming $f(E) = 1$ and $F_\infty(E) = 0$

$$g(E) = H(t)/kT \tag{11.38}$$

The determination of $g(E)$, by which $H(t)$ of (11.34) can be obtained to fit the measured $H(t)$, is described in the next section. Although the application of the transient HMC method to an isothermal mode like ICTS [75] is only briefly discussed here, this method can also be applied to a temperature-scanning mode like DLTS [78].

11.3.3 Transient HMC Measurements

Transient HMC measurements were carried out at 2 MHz for various temperatures. Only signals of $H(t)$ longer than the dielectric relaxation time are valid as mentioned in Section 11.3.2. Although the signals of $H(t)$ get saturated at a filling time τ_f (under the zero-bias condition) longer than 1 sec, they were measured at $\tau_f = 50$ sec. The signal of $H(t)$ was found to be independent of V for $V < -3$V but was found to vary with V for $V > -3$V. Because this indicates that the effect of interface states is eliminated at $V < -3$V, the transient HMC was measured at -4V.

The temperature dependence of $H(t)$ is shown in Figure 11.12 for the a-SiGe:H/p-c-Si heterojunction, and the temperature dependence of the time (t_p) at which the signal $H(t)$ becomes maximum is also inserted in this figure. A good linear relation between $\log(t_p)$ and $1/T$ was obtained, and values of $\nu_n = 1 \times 10^{12}$ s^{-1} and $E_C - E_{peak} = 0.78$ eV were estimated by using (11.37b). Figure 11.13 shows variation of the measured and the calculated $H(t)$ with measurement time. The calculated $H(t)$ was obtained from (11.34) for $\nu_n = 1 \times 10^{12}$ s^{-1}. The $g(E)$ for $E_O = 1.63$ eV shown in Figure 11.14 was used in this calculation [49]. It is

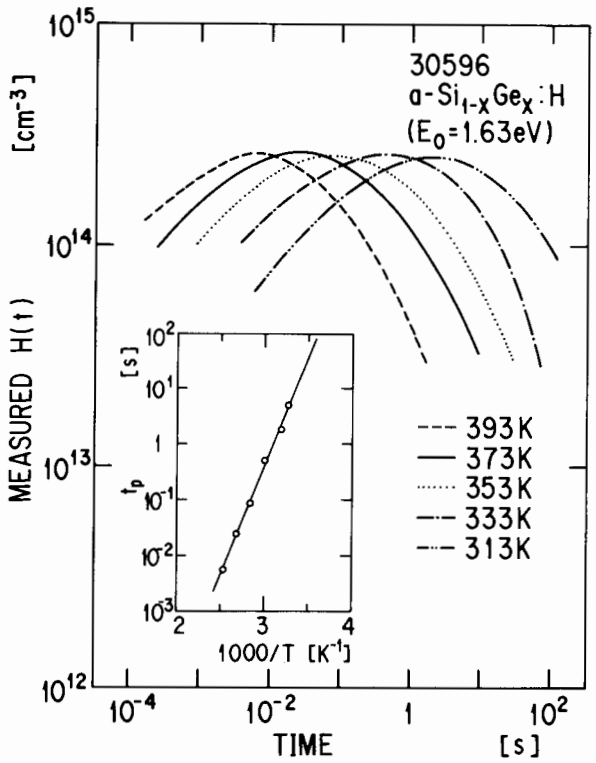

Figure 11.12 Temperature dependence of $H(t)$ for a-SiGe:H ($E_0 = 1.63$ eV)/p-c-Si heterojunction. Temperature dependence of time (t_p) at which $H(t)$ becomes maximum is given in insert [$t_f = 50$ sec and $V = -4$V]. From: [47].

clear from this figure that the calculated $H(t)$ is found to fit the measured $H(t)$ very well at each temperature.

Figure 11.14 shows the $g(E)$ estimated from the transient HMC method for different amorphous films. Here, to estimate $g(E)$, ν_n were 4×10^{12}, 8×10^{11}, 4×10^{11}, 4×10^{11}, and 8×10^{11} s^{-1} for $E_O = 1.55$, 1.70, 1.76, 1.80, and 1.88 eV, respectively. The $g(E)$ obtained in this figure were found to be (1) in good agreement with the density of singly occupied dangling bonds (D^0), and (2) unaffected by interface state density [49]. This appears to be the first systematic effort to electrically estimate $g(E)$ below the Fermi level for undoped a-Si:H/c-Si heterojunctions. The energy locations of the peak $g(E)$ for undoped materials have been found to be close to those reported by Tsutsumi [79] and Kocka [80]. A comparison between the results given in Figure 11.14 and those obtained by DLTS and ICTS methods for doped materials has been performed in [49].

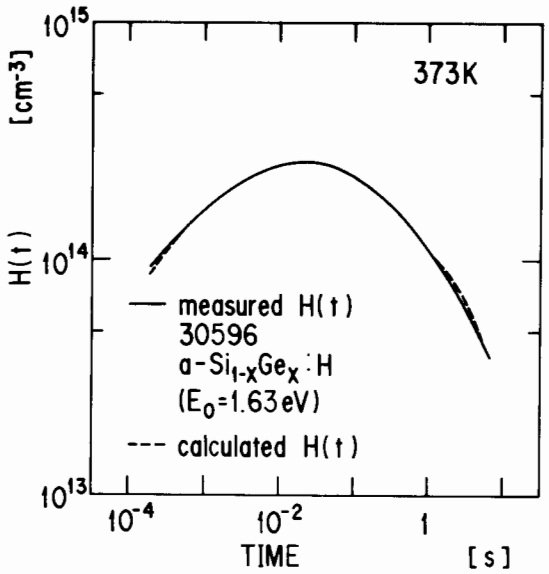

Figure 11.13 Comparison between measured and calculated $H(t)$ for a-SiGe:H (E_0 = 1.63 eV)/p-c-Si heterojunction. From: [47].

Light-induced creation of metastable defects in undoped a-Si:H has received considerable attention because it is directly associated with the degradation of the efficiency of a-Si:H solar cells [81]. Moreover, the study of thermal recovery process has been important in solving this problem. The transient HMC method enables us to measure the real-time evaluation of $g(E)$ in the 150°C annealing process because it takes only 1 sec to carry out such a measurement. Figure 11.15 shows the time-resolved $g(E)$ and the corresponding signals $H(t)$ [81]. The $H(t)$ for the as-deposited film did not change at all during the annealing process at 150°C, indicating that contact properties were not affected by thermal treatment; therefore, changes of $H(t)$ in the light-soaked film should be ascribed to the changes of the bulk $g(E)$ of undoped a-Si:H.

11.4 DARK CURRENT-VOLTAGE CHARACTERISTICS

11.4.1 Forward Current-Voltage Characteristics

Figure 11.16 shows the typical I-V characteristics in (a) log-log and (b) semilog presentations for the undoped a-Si:H/p-c-Si heterojunction. Two current transport mechanisms were proposed to explain these I-V characteristics.

1. A bulk-limited (space-charge-limited) current-transport mechanism [82, 83];
2. A junction-limited current-transport mechanism [16].

The essential difference between (1) and (2) is whether the resistance of the depletion region is greater or smaller than the resistance of the amorphous film. (In the bulk-limited case the applied bias drop is mainly across the amorphous layer; in the junction-limited case the applied bias drop is across the depletion region.) Because the resistivity and thickness of the a-Si:H were about 10^9 Ωcm and 1.2 μm, respectively, the expected current in the bulk-limited case should be about 3.3×10^{-9}A at 0.05V for an area of 0.785 mm^2. The current at forward voltages lower than 0.05V seems to be ohmic in nature because in this voltage region the $I \propto V$ [83]. The observed current, however, is much smaller than 3.3×10^{-9}A.

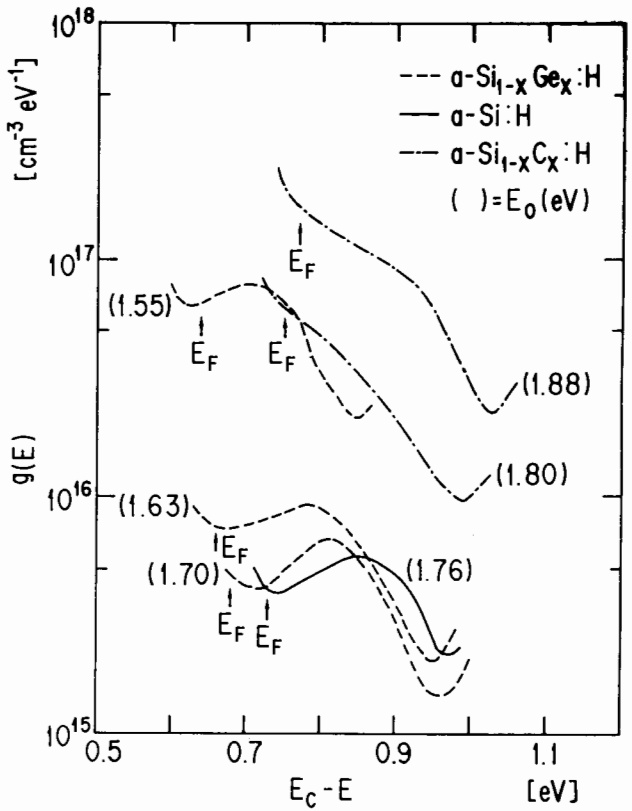

Figure 11.14 Density-of-state distribution $g(E)$ in undoped films having various optical band gaps. From: [51].

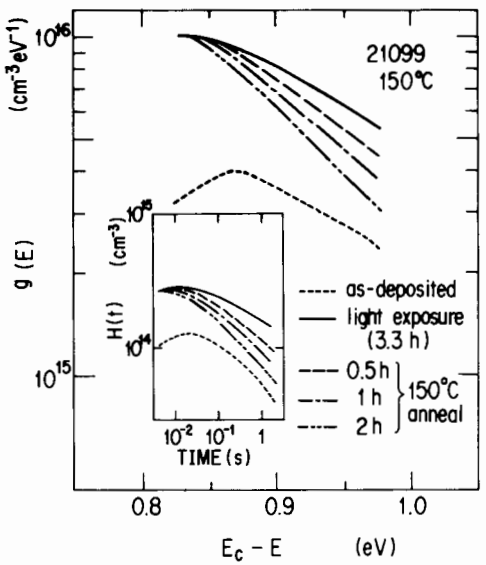

Figure 11.15 Changes of $g(E)$ at measuring temperature of 150°C. Signal $H(t)$ of transient HMC, from which $g(E)$ was calculated, is given in insert. From: [81].

Judging from the magnitude of the current, the forward current for $V < 0.4$V (close to V_B) is thought to be limited by the a-Si:H/c-Si heterojunction. The voltage dependence of the junction-limited current can be expressed by

$$I \propto \exp(AV) - 1 \tag{11.39}$$

where A is temperature independent. The forward current seems to be proportional to V in the voltage range lower than 0.05V because $\exp(AV)$ can be approximately expanded in Taylor's series $1 + AV$. Therefore, the I-V characteristics should be discussed on the basis of the junction-limited current-transport mechanism in this voltage region. Three models for explaining the current of heterojunctions are discussed: (1) A is independent of the measuring temperature (T) for a tunneling model, (2) $A = q/kT$ for a diffusion model, and (3) $A = q/2kT$ for a recombination model.

Let us consider the current transport mechanism of undoped a-Si:H/p-c-Si heterojunctions. The diode I-V characteristics for the four different resistivities of p c-Si (0.005–0.01 Ωcm for sample (a), 0.1–0.15 Ωcm for sample (b), 1–2 Ωcm for sample (c), and 5–10 Ωcm for sample (d), Figure 11.17) have been measured as a function of temperature in the range 297K to 374K. Figure 11.18 shows an

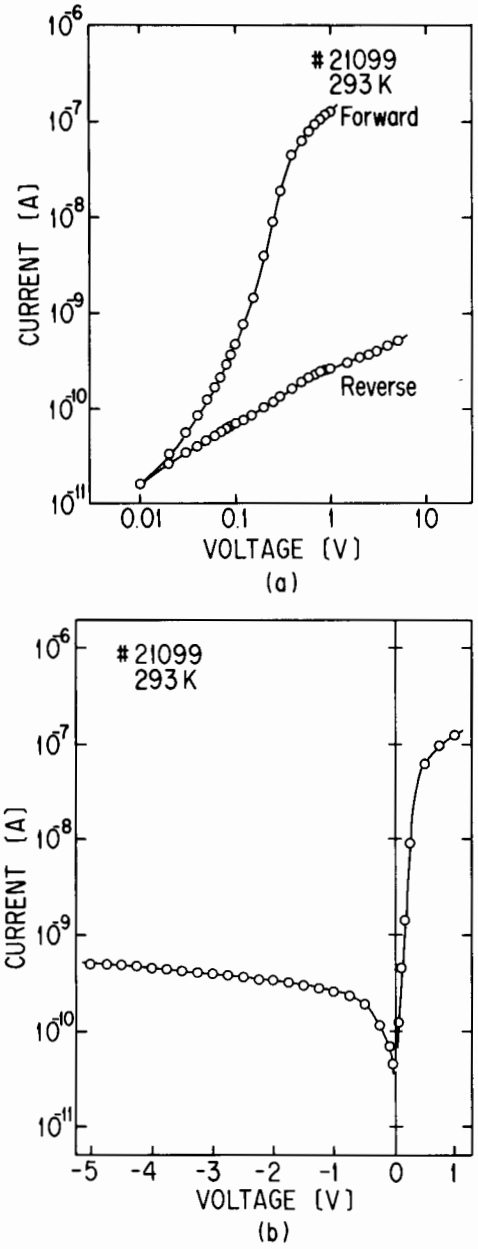

Figure 11.16 Current-voltage characteristics of undoped a-Si:H/p-c-Si ($N_A = 10^{16}$ cm^{-3}) heterojunction: (a) log I-log V plots and (b) log I-V plots. From: [48].

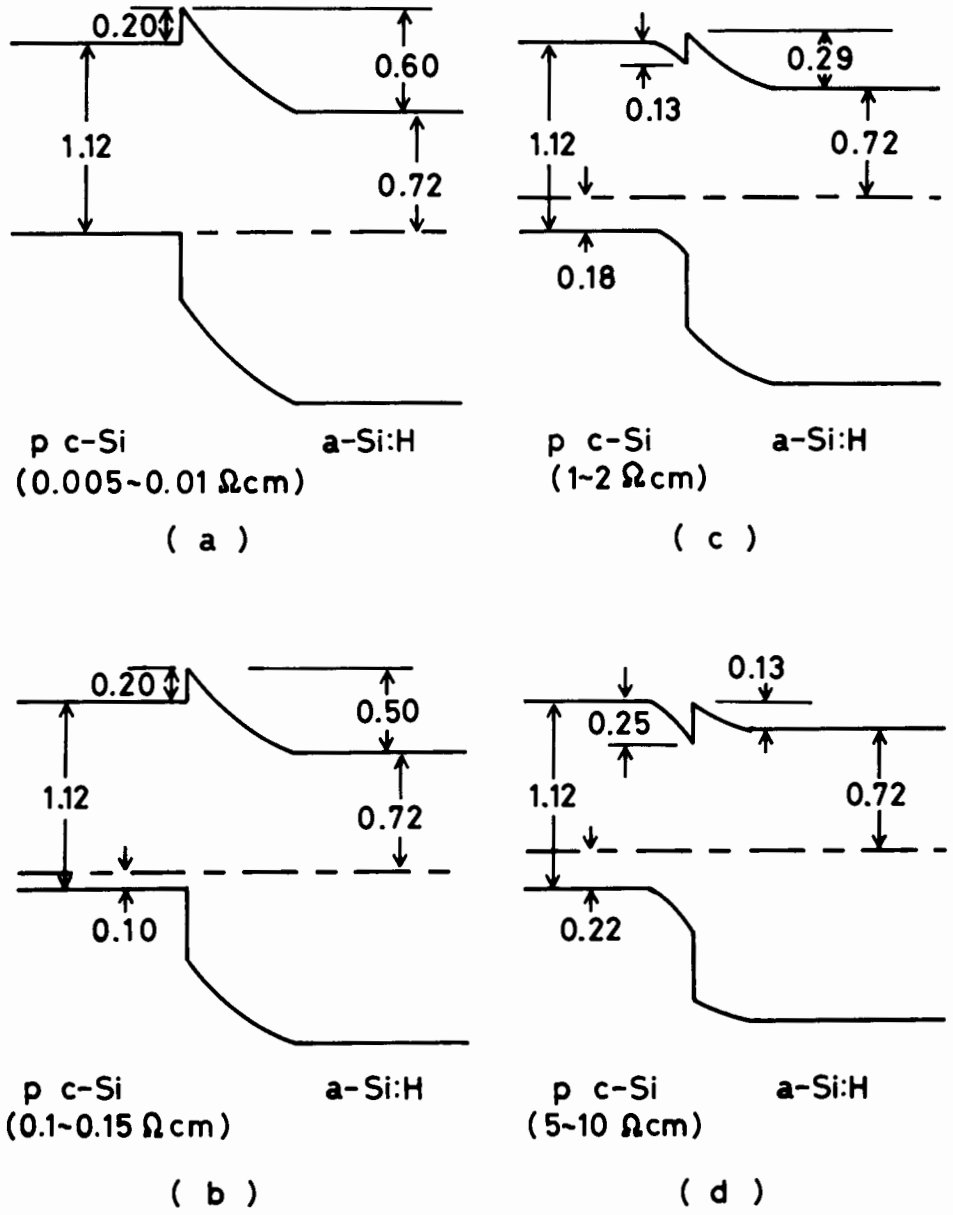

Figure 11.17 Energy-band diagrams for heterojunctions using *p*-c-Si having different resistivities. From: [16].

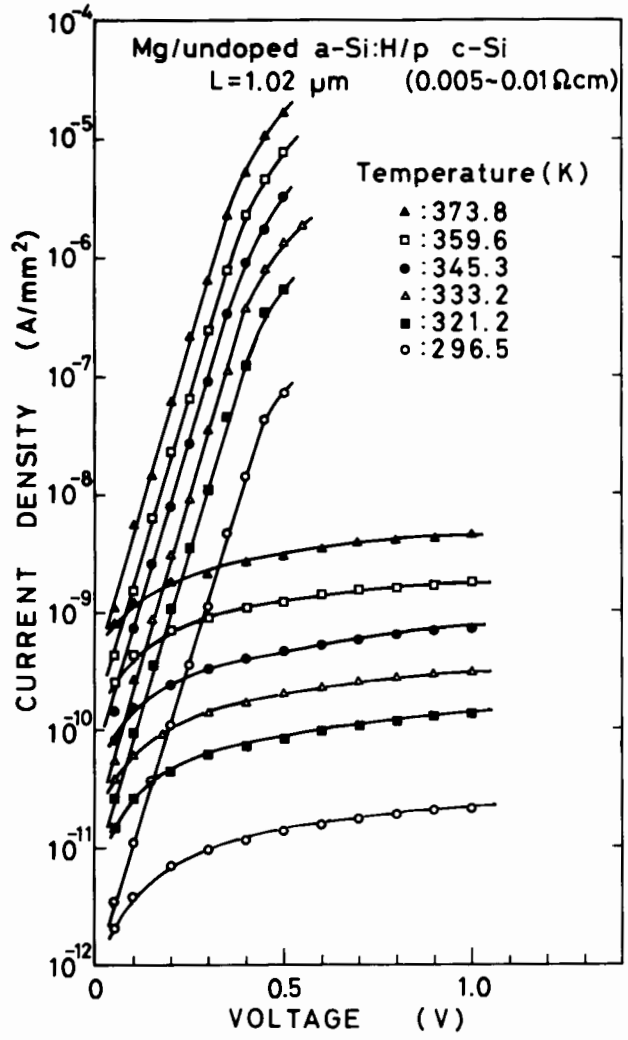

Figure 11.18 Examples of current-voltage characteristics at different temperatures of heterojunction (d) given in Figure 11.17. From: [16].

example of the temperature dependence of the *I-V* characteristics for the samples. For the other samples, experimental data can be found in the literature [16]. It is clear from the experimental results that the slope of the forward characteristics is constant for different temperatures; therefore, the current in this voltage region can be described by

$$I = I_0 \exp(AV) \tag{11.40}$$

and

$$I_0 \propto \exp(-\Delta E_{af}/kT) \tag{11.41}$$

where ΔE_{af} is the temperature-independent constant. From (11.41), ΔE_{af} were estimated to be 0.72, 0.80, 0.65, and 0.63 eV for samples (a)–(d), respectively (Figure 11.19). Since A in (11.40) is independent of temperature, the forward current must be limited by tunneling.

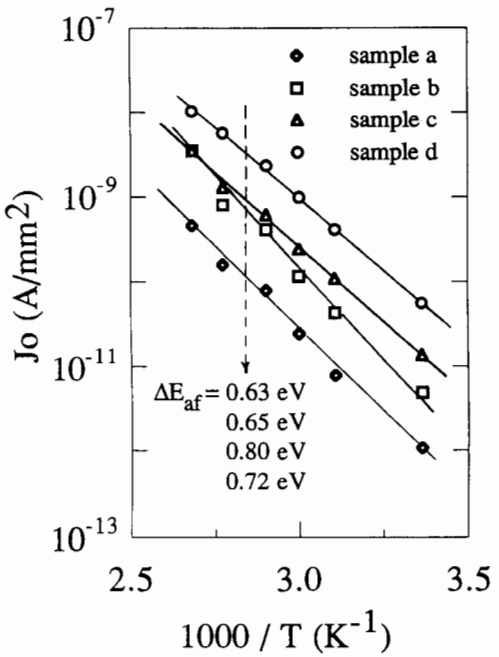

Figure 11.19 The variation of the ln I_0 versus $1/T$ for different heterojunctions given in Figure 11.17. From: [16].

Models for junction transport based on the tunneling process have been proposed by several groups, and these are schematically shown in Figure 11.20(a). To explain the present experimental results, each model is examined separately.

The simplest model consists of the tunneling of carriers through the spike-shaped barrier in the conduction band (Figure 11.20(a)). According to Riben [5],

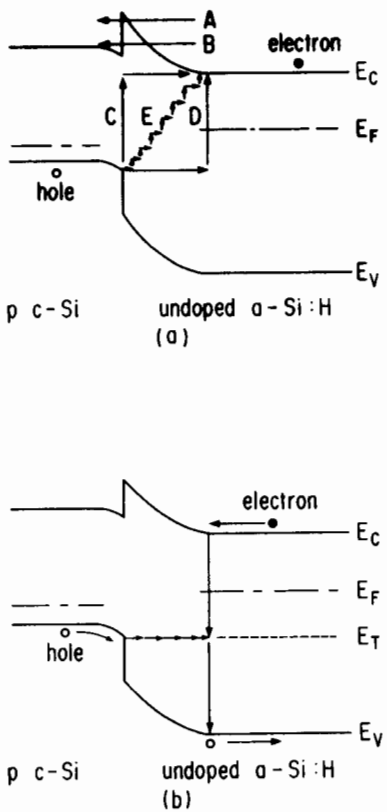

Figure 11.20 Tunneling models for heterojunctions: (a) reported tunneling models and (b) a multistep tunneling capture-emission model. From: [16].

predominant tunnel flux takes place at an energy close to the peak of the barrier within an energy difference of about 0.1 eV for crystalline heterojunctions, which is indicated by path A in the figure. In the present heterojunction, however, a tunneling process at an energy range far below the barrier peak, indicated by path B in the figure, is quite possible because the localized states are quasi-continuously distributed within the gap of a-Si:H, spatially as well as energetically. It is clear from the model that the magnitude of ΔE_{af} is expected to be larger than 1.12 eV for sample (a). This requirement contradicts the actual data, i.e., ΔE_{af} for sample (a) was obtained experimentally to be 0.72 eV.

A second model based on the tunneling of carriers was originally presented as the reason for the excess current in tunnel diodes. As has been discussed by Riben [5], one-step current tunneling (C or D in Figure 11.20(a)) is always smaller

than that multistep tunneling (E in Figure 11.20(a)). The multistep tunneling process should predominate in the present system because localized states are quasi-continuously distributed in the mobility gap. According to this multistep tunneling process, however, I_0 should change exponentially with T due to the temperature dependence of the bandgap. The I_0 obtained in this study varies exponentially with $1/T$, as shown in Figure 11.19.

In order to solve this disagreement, a multistep tunneling capture-emission process has been proposed [15, 16] as the most probable model for the present system, shown in Figure 11.20(b). A hole in the valence band of p-c-Si flows from one localized state to another in a-Si:H located within an energy range of kT by a multistep-tunneling process and keeps flowing until the tunneling rate becomes smaller than the rate for hole release from the localized state to the valence band of a-Si:H or for recombination of the hole with an electron in the conduction band of a-Si:H. An ending point of tunneling may be close to the edge of the depletion layer of a-Si:H, where the tunneling rate decreases due to a decrease of electric field.

Thus, a current flowing from p-c-Si to undoped a-Si:H is given by

$$I = B(e_p + \sigma_n v_{th} n)\exp(AV) \tag{11.42}$$

where B is a constant almost independent of applied voltage and temperature, e_p is the hole emission rate given as $e_p = \sigma_p v_{th} N_V \exp[-(E_T - E_V)/kT]$, σ_n is the capture cross section of electrons, v_{th} is the thermal velocity, n is the electron density in the conduction band of a-Si:H given by $n = N_C \exp[-(E_C - E_F)/kT]$, σ_p is the capture cross section of holes, N_V and N_C are the effective densities of states in the valence band and the conduction band of a-Si:H, respectively, and E_F, E_T, N_V, and E_C are the energies of the Fermi level, the localized state where the hole combines with an electron or emits into the valence band and the conduction band of a-Si:H, respectively. The current is described by

$$I = I_0 \exp(AV) \tag{11.43}$$

with

$$I_0 = B\{\sigma_p v_{th} N_V \exp[-(E_T - E_V)/kT] + \sigma_n v_{th} N_C \exp[-(E_C - E_F)/kT] \tag{11.44}$$

By comparing (11.33) and (11.34) with the experimental data, several possibilities can be deduced. For the junction property using the lowest resistivity p-c-Si (sample (a)), $\Delta E_{af} = 0.72$ eV was obtained. This value coincides with that of the activation energy δ_2 ($= E_C - E_F$) of the dark conductivity of undoped a-Si:H. Therefore,

considering the band diagram shown in Figure 11.17(a), the electron-capture rate is larger than the hole-emission rate, that is, the second term predominates in the right-hand side of (11.44). For the samples (b)–(d) on the other hand, the obtained values of ΔE_{af} were 0.80, 0.65, and 0.63 eV, respectively, which correlates with an increase in the substrate resistivity. This suggests that hole emission dominates for these samples, namely, the first term in the right-hand side of (11.44) determines the magnitude of I_0. The multistep capture-emission model has been supported [26, 45] and has been applied to B-doped a-Si:H/n-c-Si and B-doped a-Si:H/n-c-GaAs heterojunctions [20].

11.4.2 Reverse Current-Voltage Characteristics

The a-Si:H/c-Si heterojunction can keep a small dark current even at higher reverse bias, as it is shown in Figure 11.16. From (11.29) and (11.30), the saturated value of the reverse current is expected to be I_0. However, the reverse current exceeds the value of I_0, indicating that the reverse current should be limited by another transport mechanism.

Figure 11.21 shows the reverse current as a function of $(V_B - V)^{1/2}$, which is replotted from the data given in Figure 11.16. When the generation current is taken into account in the depletion region, this current should be proportional to

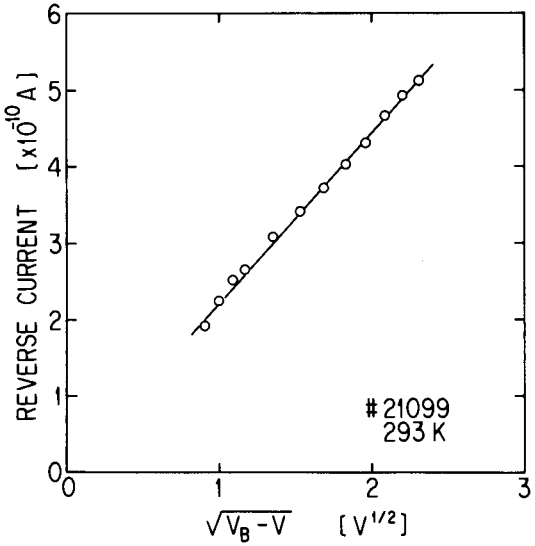

Figure 11.21 Reverse current as a function of $(V_B - V)^{1/2}$ where V_B is 0.35V. From: [88].

the width of the depletion region that varies with $(V_B - V)^{1/2}$. The data show a good linearity in the range of $-5V < V < -0.5V$, indicating that this reverse current should be limited by the generation current in the depletion region. In sample (a), the depletion region exists only on the a-Si:H side because the *p*-c-Si is a heavily B-doped c-Si. This proportionality between reverse current and $(V_B - V)^{1/2}$ is held throughout the studied temperature range, indicating that a generation current is produced in the depletion region of a-Si:H under reverse bias condition.

The reverse current is an increasing function of the c-Si resistivity [16]. Because the width of the depletion region in c-Si is proportional to the resistivity of c-Si, it is clear from (11.15) that the generation current should increase with an increase of the c-Si resistivity, which is experimentally observed. Therefore, the main generation current is produced in the depletion region of c-Si except for the sample (a). Furthermore, the generation current per unit volume in the depletion region of c-Si is greater than that in the depletion region of a-Si:H. This should be important when discussing the magnitude of the leakage current (the drain current in the off-state) in thin-film transistors made of a-Si:H or polycrystalline (or crystalline) silicon, because this current is believed to originate from the electron-hole pair generation in the reverse-biased drain junction [85, 86] of the thin-film transistor.

The reverse current of *p*-a-Si:H/*n*-c-Si heterojunction was also investigated in detail by Mimura and Hatanaka by measuring the *I-V* and *C-V* characteristics [23]. In this work, it was revealed that there is interface defect that will obstruct the spread of the depletion layer in c-Si at the a-Si:H/c-Si interface. These interface-defect states will assist the generation of the reverse current in the *p*-Si:H/*n*-c-Si heterojunction [23].

11.5 APPLICATIONS OF AMORPHOUS/CRYSTALLINE HETEROJUNCTIONS

11.5.1 Vidicon Targets Without a *p-n* Diode Array

An ultrahigh photosensitive *silicon-intensifier target* (SIT) image-pickup tube with *p-n* diode-arrayed c-Si target has been used widely. However, it is known that the conventional SIT tube with a *p-n* diode-arrayed c-Si target has several disadvantages. Among them are (1) blooming effect due to the diffusion of excess carriers into adjacent *p-n* diodes, (2) low resolution limited by the pitch of the diode array, and (3) the picture defects introduced in the fabrication process, which includes a high-temperature process for making the *p-n* junctions. As a matter of course, the heterojunction targets such as c-Si/CdTe and c-Si/Sb_2S_3 without a diode array were proposed, but these heterojunctions did not exhibit sufficiently good rectifying properties to get a high photo-to-dark current ratio.

The a-Si:H/c-Si heterojunction has the advantages of (1) good rectifying property, indicating a small dark current under a large reverse-bias condition and (2) the depletion region in c-Si, where the electron-hole separation takes place, spreading widely in the reverse-bias condition, resulting in a large photocurrent. These are the advantages for getting a high *signal-to-noise* (S/N) ratio. In addition to the advantages in the action mechanism, the low-temperature process for the fabrication of the heterojunction is another advantage preventing defect formation in c-Si.

The vidicon target having an a-Si:H/c-Si heterojunction has been investigated, and the actual reported values for this kind of vidicon [30] are described here briefly. The dark reverse current and sensitivity were 10 nA/lx and 430 nA/lx respectively, at $-6V$. These reach the values of well-defined c-Si targets with the *p-n* diode array. The horizontal resolution attained was more than 800 television lines; the picture had few defects, no blooming, and no evident burning. These properties are superior to those obtained for the conventional c-Si vidicon target. More details about the image-pickup tube can be found in Chapter 15.

11.5.2 Gamma-Ray Detectors

A γ-ray detector requires a high absorption coefficient for γ-ray, a wide depletion region, and a small, dark reverse current. Although crystalline semiconductors (c-Ge, c-HgTe, and c-GaAs) consisting of atoms having heavy masses are suitable for γ-ray absorption at the present stage, c-Si is considered the appropriate material for the γ-ray (< 100 keV) detector. This is due to the fact that, with c-Si, it is easy to get a small, dark reverse current as well as a wide depletion region because of its ultralow impurity and defect levels; however, a high-temperature process is required, such as solid-state diffusion of impurities or ion implantation, followed by annealing to form a *p-n* homojunction. This high-temperature process produces additional defects in ultrahigh purity c-Si, resulting in an increase of the dark reverse current and a decrease in the width of the depletion region.

The a-Si:H/c-Si heterojunction γ-ray detector may have some advantages over c-Si heterojunction. The low processing temperature, simple fabrication process, and good junction properties are very attractive in a-Si:H/c-Si heterojunction. Undoped a-Si:H/*p*-c-Si heterojunctional γ-ray detectors were fabricated, and their electrical characteristics were reported [31] to be comparable to c-Si detectors with a *p-n* homojunction. More details about the γ-ray detectors can be found in Volume 1 of this book.

11.5.3 Solar Cells

Amorphous/crystalline heterojunction solar cells which are similar to *Schottky barrier* (SB) and *metal-thin insulator-semiconductor* (MIS) solar cells, have advantages such as simple, low-temperature fabrication processes, resulting in low-cost fabrication. To improve a low open-circuit voltage in SB solar cells, a very thin oxide

layer (abut 20Å) is needed between the metal and the semiconductor [87]. However, it is quite difficult to control the thickness of such a thin oxide layer. It is expected from this point of view that the amorphous/crystalline heterojunction solar cell should show reproducible and stable properties, because this type of cell does not require any oxide inter-layer.

Different types of heterojunction solar cells have been reported [32]. In B-doped a-SiC:H/*n*-c-Si solar cells [34], the open-circuit voltage of 0.54V, the short-circuit current of 30 mA/cm^2, and efficiency of 11.38% under AM1 light (100 mW/cm^2) were achieved.

11.5.4 Heterojunction Bipolar Transistors (HBT)

The advantages of HBT with a wide band gap emitter arise from the band discontinuities (ΔE_V and ΔE_C) between the two semiconductors. Because the large barrier in valence band between a-Si:H and c-Si effectively prevents any holes from flowing into the a-Si:H, the base doping level can be higher (i.e., the base resistance can be lower) and the emitter doping level can be lower (i.e., the emitter capacitance can be lower). A high common-emitter-current gain (η_{FE}) is obtained, because an injection efficiency is approaching unity due to the above merit.

In general, the frequency response of transistors is limited by the carrier-transit time through the base layer. The HBT, in this sense, shows the advantage of high-speed operation, because the base layer can be designed to be thinner due to its higher doping level. High-speed HBT with a crystalline/crystalline heterojunction was used in the field of Si-LSI. However, c-GaP emitter acts as a source of undesirable dopants for c-Si, and c-SiC emitter shows a large lattice mismatch with c-Si. Because the dopant of the base layer is diffused during the high-temperature growth process of an emitter, a low-temperature process for fabricating an emitter on c-Si is strongly desired. Therefore, a-Si:H or a-SiC:H is thought to be a suitable material for a wide-bandgap emitter. Using the *n*-a-Si:H/*p*-c-Si/*n* c-Si, a maximum η_{FE} was reported to be 14 at a base *Gummel number* (GN) of 1.35×10^{12} s/cm^4 [35]. In the case of an *n* a-SiC:H emitter instead of a-Si:H, a maximum η_{FE} of 120 at GN of about 10^{12} s/cm^4 was also reported [38]. Although the large barrier in the valence band did not completely block the flow of holes from the base into the emitter, these HBT exceeded Si homojunction transistors in η_{FE}. However, the high resistance of the amorphous emitter has some disadvantages, resulting in the reduction of the collector current density and the reduction of high-frequency characteristics. To avoid these problems, hydrogenated microcrystalline Si (μc-Si:H) or hydrogenated microcrystalline silicon-carbon alloys (μc-SiC:H) with microcrystalline Si have been investigated as a wide-bandgap emitter [39, 42–44] and an improved HBT structure has been proposed [46]. Details about this type of HBT are described in Chapter 12.

11.6 CONCLUSION

This chapter has described the properties and applications of heterojunctions consisting of hydrogenated amorphous silicon-based alloys and crystalline silicon. Capacitance-voltage characteristics and transient capacitance of amorphous/crystalline heterojunctions have been discussed theoretically as well as experimentally. Although those properties strongly depend on the dielectric relaxation and trapping/detrapping processes, the capacitance-voltage characteristics measured at frequencies higher than $\sigma_2/2\pi\epsilon_{s2}$ can easily be explained theoretically. Therefore, in this chapter we have focused on high-frequency properties of the heterojunction. Through these studies, the determination methods for the gap-state densities and profiles near the midgap in undoped (highly resistive) films have been proposed. Current-voltage characteristics of amorphous/crystalline heterojunctions have also been described experimentally, and the current transport mechanisms have been discussed.

The major advantage of amorphous/crystalline heterojunctions mentioned in this chapter is a low-temperature ($\leq$300°C) fabrication process. Those heterojunctions (especially a-Si:H/c-Si heterojunctions) have junction properties suitable for a variety of device applications using advantages such as (1) a high forward-to-reverse current ratio, (2) a small dark current even at a large reverse-bias condition, (3) wide depletion regions in both a-Si:H and c-Si, and (4) large valence band and small conduction band discontinuities between a-Si:H and c-Si. Vidicon targets and γ-ray detectors make good uses of (2) and (3), solar cells of (1) and (3), and *n-p-n* HBT of (1) and (4).

ACKNOWLEDGMENTS

The authors wish to express their gratitude to Dr. K. Tanaka, Dr. A. Matsuda, Y. Toyoshima, and other members of the staff of the Non-Equilibrium Materials Section in the Electrotechnical Laboratory for their valuable insights and comments.

REFERENCES

[1] Milnes, A. G., and D. L. Feucht, *Heterojunctions and Metal-Semiconductor Junctions*, Academic Press, New York, 1972.

[2] Anderson, R. L., "Experiments on Ge-GaAs heterojunctions," *Solid-State Electron.*, *Vol. 5*, 1962, pp. 341–351.

[3] Rediker, R. H., S. Stopek, and J. H. R. Ward, "Interface-alloy epitaxial heterojunctions," *Solid-State Electron.*, *Vol. 7*, 1964, pp. 621–629.

[4] Hampshire, M. J., and G. T. Wright, "The silicon-germanium *n-p* heterojunction," *Brit. J. Appl. Phys., Vol. 15*, 1964, pp. 1331–1340.

[5] Riben, A. R., and D. L. Feucht, "*n*Ge-*p*GaAs heterojunctions," *Solid-State Electron., Vol. 9*, 1966, pp. 1055–1065.

[6] Riben, A. R., and D. L. Feucht, "Electrical transport in nGe-pGaAs heterojunctions," *Int. J. Electron., Vol. 20*, No. 6, 1966, pp. 583–599.

[7] Donnelly, J. P., and A. G. Milnes, "Current/voltage characteristics of p-n Ge-Si and Ge-GaAs heterojunctions," *Proc. IEE, Vol. 113*, No. 9, 1966, pp. 1468–1476.

[8] Kroemer, H., "Theory of a wide-gap emitter for transistors," *Proc. IRE, Vol. 45*, 1957, pp. 1535–1537.

[9] Rediker, R. H., T. M. Quist, and B. Lax, "High speed heterojunction photodiode and beam-of-light transistors," *Proc. IEEE, Vol. 51*, 1963, pp. 218–219.

[10] Kroemer, H., "A proposed class of heterojunction injection lasers," *Proc. IEEE, Vol. 51*, 1963, pp. 1782–1783.

[11] Tawada, Y., M. Kondo, H. Okamoto, and Y. Hamakawa, "a-SiC:H/a-Si:H heterojunction solar cell having more than 7.5% conversion efficiency," *Proc. 15th IEEE Photovoltaic Specialists Conf.*, Florida, 1981, pp. 245–246.

[12] Grigorovici, R., N. Croitoru, A. Devenyi, and E. Teleman, "Band structure and electrical conductivity in amorphous germanium," Proc. Int. Conf. Semiconductors, Paris, 1964, pp. 432–428.

[13] Stourac, L., "Amorphous-crystalline heterojunctions," Proc. Int. Conf. Amorphous Semiconductors, Bucharest, 1982, pp. 104–109.

[14] Spear, W. E., and P. G. LeComber, "Electronic properties of substitutionary doped amorphous Si and Ge," *Phil. Mag., Vol. 33*, No. 6, 1976, pp. 935–949.

[15] Matsuura, H., T. Okuno, H. Okushi, N. Hata, S. Yamasaki, H. Oheda, A. Matsuda, and K. Tanaka, "Electrical properties of *n-p* amorphous-crystalline silicon heterojunctions," *Extended Abstracts of 15th Conf. on Solid State Devices and Materials*," Tokyo, 1983, pp. 185–188.

[16] Matsuura, H., T. Okuno, H. Okushi, and K. Tanaka, "Electrical properties of *n*-amorphous/*p*-crystalline silicon heterojunctions," *J. Appl. Phys., Vol. 55*, No. 4, 1984, pp. 1012–1019.

[17] Rahman, M. M., and S. Furukawa, "Preparation and electrical properties of an amorphous SiC/crystalline Si p^+-*n* heterostructure," *Jpn. J. Appl. Phys., Vol. 23*, No. 5, 1984, pp. 515–524.

[18] Mimura, H., and Y. Hatanaka, "Optoelectrical properties of amorphous-crystalline heterojunctions," *Appl. Phys. Lett., Vol. 45*, 1984, pp. 452–454.

[19] Rubinelli, F. A., S. Albornoz, and R. H. Buitrago, "An approach to *p-n* amorphous-polycrystalline silicon heterojunction solar cell," *Technical Digest of Int. PVSEC-1*, Kobe, 1984, pp. 115–118.

[20] Mimura, H., and Y. Hatanaka, "Electrical properties of *p*-type hydrogenated amorphous silicon-*n*-type crystalline gallium arsenide heterojunctions," *Jpn. J. Appl. Phys., Vol. 24*, No. 5, 1985, pp. L355–L357.

[21] Rubinelli, F. A., S. Albornoz, and R. H. Buitrago, "Amorphous-crystalline silicon isotype heterojunction: Electrostatic potential distribution and $C(V)$ curves," *Solid-State Electron., Vol. 28*, No. 8, 1985, pp. 741–750.

[22] Wang, W., and K. Liao, "The photosensitivity of a-Si:H/p^+ *p* c-Si heterojunction," *Mat. Res. Soc. Symp. Proc., Vol. 70*, 1986, pp. 399–402.

[23] Mimura, H., and Y. Hatanaka, "Reverse current characteristics of hydrogenated amorphous silicon-crystalline silicon heterojunctions," *Jpn. J. Appl. Phys., Vol. 26*, No. 1, 1987, pp. 60–65.

[24] Rubinelli, F. A., M. R. Battioni, and R. H. Buitrago, "Distribution of the electrostatic potential barrier in the n-p, amorphous-crystalline silicon heterojunction," *J. Appl. Phys., Vol. 61*, No. 2, 1987, pp. 650–658.

[25] Rubinelli, F. A., "Theoretical $C(V)$ equation of an amorphous-crystalline heterojunction at low frequency," *Solid-State Electron., Vol. 30*, No. 6, 1987, pp. 593–599.

[26] Xu, Z. Y., W. Chen, B. F. Zhao, C. A. Wang, F. A. Zhang, and J. Y. Wang, "The effect of the gap DOS in a-Si on the properties of the a-Si/c-Si heterojunction," *Journal of Non-Crystalline Solids, Vols. 97, 98*, 1987, pp. 983–986.

[27] Meikle, S. G., and Y. Hatanaka, "Characteristics of the hydrogenated amorphous silicon-crystalline cadmium telluride heterojunction diode," *Jpn. J. Appl. Phys., Vol. 26*, No. 11, 1987, pp. L1812–L1814.

[28] Essick, J. M., and J. D. Cohen, "Investigation of amorphous-crystalline silicon interface via capacitance techniques," *Mat. Res. Soc. Symp., Vol. 118*, 1988, pp. 549–554.

[29] Mimura, H., and Y. Hatanaka, "A new silicon vidicon target using an amorphous-crystalline silicon heterojunction," *Extended Abstracts of 17th Conf. on Solid State Devices and Materials*, Tokyo, 1985, pp. 115–118.

[30] Mimura, H., and Y. Hatanaka, "The use of amorphous-crystalline silicon heterojunctions for the application to an imaging device," *J. Appl. Phys., Vol. 61*, No. 7, 1987, pp. 2575–2580.

[31] Yabe, M., N. Sato, and Y. Seki, "A new silicon nuclear radiation detector using a-Si:H/c-Si heterojunction," *Proc. 4th Sensor Symposium*, Tsukuba, 1984, pp. 105–109.

[32] Okuda, K., H. Okamoto, and Y. Hamakawa, "Amorphous Si/polycrystalline Si stacked solar cell having more than 12% conversion efficiency," *Jpn. J. Appl. Phys., Vol. 22*, No. 9, 1983, pp. L605–L607.

[33] Rahman, M. M., and S. Furukawa, "Amorphous/crystalline heterostructure as a novel approach to fabrication of a solar cell," *Electron. Lett., Vol. 20*, No. 2, 1984, pp. 57–58.

[34] Rahman, M. M., and S. Furukawa, "Preparation and performance of a novel structure amorphous SiC/crystalline Si solar cell," *Technical Digest of Int. PVSEC-1*, Kobe, 1984, pp. 171–174.

[35] Ghannam, M., J. Nijs, R. Mertens, and R. Dekeersmaecker, "A silicon bipolar transistor with a hydrogenated amorphous emitter," *Technical Digest of Int. Electron Devices Meeting*, San Francisco, 1984, pp. 746–748.

[36] Sasaki, K., M. M. Rahman, and S. Furukawa, "An amorphous SiC:H emitter heterojunction bipolar transistor," *IEEE Electron Device Lett., Vol. EDL-6*, No. 6, 1985, pp. 311–312.

[37] Sasaki, K., S. Furukawa, and M. M. Rahman, "A new Si bipolar transistor using amorphous SiC:H as a wide-gap emitter," *Extended Abstracts of 17th Conf. on Solid State Devices and Materials*, Tokyo, 1985, pp. 385–388.

[38] Sasaki, K., S. Furukawa, and M. M. Rahman, "A novel structure amorphous SiC emitter HBT using low temperature process," *Technical Digest of Int. Electron Devices Meeting*, Washington, 1985, pp. 294–297.

[39] Symons, J., M. Ghannam, J. Nijs, A. van Ammel, P. de Schepper, A. Neugroschel, and R. Mertens, "The use of amorphous and microcrystalline silicon for silicon heterojunction bipolar transistors," *Appl. Phys. A, Vol. 41*, 1986, pp. 291–295.

[40] Sasaki, K., M. Morikawa, and S. Furukawa, "Estimations of emitter crowding effect and emitter Gummel number of amorphous SiC:H emitter HBT," *Trans. IECE of Japan, Vol. E69*, No. 4, 1986, pp. 241–242.

[41] Sasaki, K., and S. Furukawa, "High current gain amorphous SiC *npn* HBT with temperature stable current gain," *Extended Abstracts of 18th Conf. on Solid State Devices and Materials*, Tokyo, 1986, pp. 291–294.

[42] Symons, J., K. Baert, J. Nijs, and R. Mertens, "Amorphous and microcrystalline silicon bipolar heterojunction transistors," *Journal of Non-Crystalline Solids, Vols. 97, 98*, 1987, pp. 1315–1318.

[43] Symons, J., M. Ghannam, A. Neugroschel, J. Nijs, and R. Mertens, "Silicon heterojunction bipolar transistors with amorphous and microcrystalline emitters," *Solid-State Electron., Vol. 30*, No. 11, 1987, pp. 1143–1145.

[44] Sasaki, K., T. Fukazawa, and S. Furukawa, "Micro-crystalline hetero-emitter with high injection efficiency for Si HBT," *Technical Digest of Int. Electron Devices Meeting*, Washington, 1987, pp. 186–189.

[45] Symons, J., J. Nijs, and R. Mertens, "The interface current in silicon bipolar transistors with emitters deposited by plasma CVD," *Proc. of Int. Topical Conf. on Hydrogenated Amorphous Silicon Devices and Technology*, Yorktown Height, 1988, pp. 159–162.

[46] Zhu, E. J., S. S. Zhang, W. W. Sheng, B. Z. Zhao, C. K. Xiong, and Y. S. Wang, "Amorphous Si/Si heterojunction microwave transistors," *IEEE Electron Device Lett.*, *Vol. 10*, No. 1, 1989, pp. 46.

[47] Kuwagaki, M., K. Imai, T. Ogino, and Y. Amemiya, "Silicon HBT with a low-resistivity amorphous SiC_x emitter," *Jpn. J. Appl. Phys.*, *Vol. 28*, No. 2, 1989, pp. L173–L175.

[48] Matsuura, H., "Density-of-state distribution for undoped a-Si:H and a-$Si_{1-x}Ge_x$:H determined by transient heterojunction-monitored capacitance method," *Jpn. J. Appl. Phys.*, *Vol. 27*, No. 4, 1988, pp. L516–L518.

[49] Matsuura, H., "A novel method for determining the gap-state profile and its application to amorphous $Si_{1-x}Ge_x$:H films," *J. Appl. Phys.*, *Vol. 64*, No. 4, 1988, pp. 1964–1973.

[50] Matsuura, H. and K. Tanaka, "The density-of-state distribution in undoped a-Si:H and a-SiGe:H determined by heterojunction with c-Si," *Mat. Res. Soc. Symp. Proc.*, *Vol. 118*, 1988, pp. 647–652.

[51] Matsuura, H., Z E. Smith, A. Matsuda, S. Yokoyama, M. Tanaka, M. Ueda, and K. Tanaka, "Midgap-state profiles in undoped amorphous silicon-based alloys," *Phil. Mag. Lett.*, *Vol. 59*, No. 2, 1989, pp. 109–114.

[52] Matsuura, H., A. Matsuda, H. Okushi, T. Okuno, and K. Tanaka, "Metal-semiconductor junctions and amorphous crystalline heterojunctions using B-doped hydrogenated amorphous silicon," *Appl. Phys. Lett.*, *Vol. 45*, No. 4, 1984, pp. 433–435.

[53] Matsuura, H., T. Okuno, H. Okushi, S. Yamasaki, A. Matsuda, N. Hata, H. Oheda, and K. Tanaka, "Ohmic contact properties of magnesium evaporated onto undoped and P-doped a-Si:H," *Jpn. J. Appl. Phys.*, *Vol. 22*, No. 3, 1983, pp. L197–L199.

[54] Matsuura, H., and H. Okushi, "Schottky barrier junctions of hydrogenated amorphous silicon-germanium alloys," *J. Appl. Phys.*, *Vol. 62*, No. 7, 1987, pp. 2871–2879.

[55] Yamasaki, S., H. Oheda, A. Matsuda, H. Okushi, and K. Tanaka, "Gap-state profiles of a-Si:H deduced from below-gap optical absorption," *Jpn. J. Appl. Phys.*, *Vol. 21*, No. 9, 1982, pp. L539–L541.

[56] Hyun, C. H., M. S. Shur, and A. Madan, "DLTS response due to localized states in hydrogenated amorphous silicon," *Journal of Non-Crystalline Solids*, *Vol. 46*, 1981, pp. 221–234. 1964–1973.

[57] Rhoderick, E. H., and R. H. Williams, *Metal-Semiconductor Contacts*, 2nd edition, Oxford University Press, Oxford, 1988, pp. 162–179.

[58] Suzuki, T., Y. Osaka, and M. Hirose, "Theoretical interpretation of capacitance-voltage characteristics of metal-a-Si:H Schottky barriers," *Jpn. J. Appl. Phys.*, *Vol. 22*, No. 5, 1983, pp. 785–788.

[59] Dohler, G. H., and M. Hirose, "Determination of the electronic density of states in amorphous semiconductors from capacitance-voltage measurements," *Proc. 2nd Conf. on Amorphous and Liquid Semiconductors*, University of Edinburgh, 1977, pp. 372–378.

[60] Singh, J., and M. H. Cohen, "Capacitance-voltage measurements in amorphous Schottky barriers," *J. Appl. Phys.*, *Vol. 51*, No. 1, 1980, pp. 413–418.

[61] Viktorivitch, P., and G. Moddel, "Interpretation of the conductance and capacitance frequency dependence of hydrogenated amorphous Schottky barrier diodes," *J. Appl. Phys.*, *Vol. 51*, No. 9, 1980, pp. 4847–4854.

[62] Michelson, C. E., A. G. Gelatos, and J. D. Cohen, "Drive-level capacitance profiling: Its application to determining gap state densities in hydrogenated amorphous silicon films," *Appl. Phys. Lett.*, *Vol. 47*, No. 4, 1985, pp. 412–414.

[63] Matsuura, H., "Density of mid-gap states for undoped a-$Si_{1-x}Ge_x$:H and a-Si:H determined by steady-state heterojunction-monitored capacitance method," *Jpn. J. Appl. Phys.*, *Vol. 27*, No. 4, 1988, pp. L513–L515.

[64] Sasaki, G., S. Fujita, and A. Sasaki, "Gap-states measurement of chemically vapor-deposited amorphous silicon: High-frequency capacitance-voltage method," *J. Appl. Phys.*, *Vol. 53*, No. 2, 1982, pp. 1013–1017.

[65] Sasaki, T., G. Sasaki, and A. Sasaki, "Some problems in determination of gap-state density in amorphous silicon," *Solar Energy Materials*, *Vol. 8*, 1982, pp. 293–302.

[66] Sze, S. M., *Physics of Semiconductor Devices*, 2nd edition, Wiley-Interscience, New York, 1981, pp. 366–369.

[67] Gelatos, A. V., and J. Kanicki, "Investigation of the silicon nitride on hydrogenated amorphous silicon interface," *Mat. Res. Soc. Symp.*, *Vol. 149*, 1989, pp. 729–734.

[68] Mimura, H., and Y. Hatanaka, "Energy-band discontinuities in a heterojunction of amorphous hydrogenated Si and crystalline Si measured by internal photoemission," *Appl. Phys. Lett.*, *Vol. 50*, No. 6, 1987, pp. 326–328.

[69] Mott, N., "Conductivity, localization, and the mobility edge," in *The Physics of Hydrogenated Amorphous Silicon II*, J. D. Joannopoulos and G. Lucovsky, eds., Springer-Verlag, New York, 1984, pp. 167–193.

[70] Sharma, D. K., and K. L. Narasimhan, "Analysis of high-frequency capacitance of amorphous silicon-crystalline silicon heterojunction," *Phil. Mag. B*, *Vol. 63*, No. 2, 1991, pp. 543–550.

[71] Cuniot, M., and Y. Marfaing, "Study of the band discontinuities at the a-Si:H/c-Si interface by internal photoemission," *Journal of Non-Crystalline Solids*, *Vols. 77, 78*, 1985, pp. 987–990.

[72] Cuniot, M., and Y. Marfaing, "Energy band diagram of the a-Si:H/c-Si interface as determined by internal photoemission," *Phil. Mag. B*, *Vol. 57*, No. 2, 1988, pp. 291–300.

[73] Patella, F., F. Evangelisti, P. Fiorini, P. Perfetti, C. Quaresima, M. K. Kelly, R. A. Riedel, and G. Margaritondo, "Photoemission studies of amorphous silicon heterostructures," *Proc. Conf. on Optical Effects in Amorphous Semiconductors*, Salt Lake City, 1984, pp. 402–409.

[74] Lang, D. V., J. D. Cohen, and J. P. Harbison, "Measurement of the density of gap states in hydrogenated amorphous silicon by space charge spectroscopy," *Physical Review B*, *Vol. 25*, No. 8, 1982, pp. 5285–5320.

[75] Okushi, H. "Gap states in phosphorus-doped amorphous silicon studied by isothermal capacitance transient spectroscopy," *Phil. Mag. B*, *Vol. 52*, No. 1, 1985, pp. 33–57.

[76] Gelatos, A. V., and J. D. Cohen, "Assessment of lattice relaxation effects in transitions from mobility gap states in hydrogenated amorphous silicon using transient photocapacitance techniques," *Appl. Phys. Lett.*, *Vol. 49*, No. 12, 1986, pp. 722–724.

[77] Gelatos, A. V., and J. Kanicki, "Direct observation of the silicon nitride on amorphous silicon interface states," *Appl. Phys. Lett.*, *Vol. 56*, No. 10, 1989, pp. 940–942.

[78] Wang, J., Q. S. Sun, H. N. Liu, and Y. L. He, "Photo-induced density-of-states variation measured by DLTS method in intrinsic micro-crystalline silicon (i-, μc-Si:H) films," *AIP Conf. Proc. on Stability of Amorphous Silicon Alloy Materials and Devices*, *Vol. 157*, American Institute of Physics, Palo Alto, 1987, pp. 82–86.

[79] Tsutsumi, Y., S. Sakata, K. Abe, Y. Nitta, H. Okamoto, and Y. Hamakawa, "Study of gap states in SiGe:H alloy system by below-gap modulated photocurrent spectroscopy," *Journal of Non-Crystalline Solids*, *Vols. 97, 98*, 1987, pp. 1063–1066.

[80] Kocka, J., M. Vanecek, and F. Schauer, "a-Si:H gap states investigated by CPM and SCLC," *Journal of Non-Crystalline Solids*, *Vols. 97, 98*, 1987, pp. 715–722.

[81] Matsuura, H., "Thermal recovery process of the midgap-state profile of light-soaked undoped hydrogenated amorphous silicon," *Appl. Phys. Lett.*, *Vol. 54*, No. 4, 1989, pp. 344–346.

[82] Schauer, F., V. Smid, O. Zmevskal, and L. Stourach, "Evaluation of space-charge-limited currents in a-Si:H/c-Si heterojunction," *Phys. Stat. Sol.*, *Vol. 73*, 1982, pp. K199–K203.

[83] Smid, V., J. J. Mares, L. Stourach, and J. Kristofik, "Amorphous-crystalline heterojunctions," in *Tetrahedrally-Bonded Amorphous Semiconductors*, D. Adler and H. Fritzsche, eds., Plenum Press, New York, 1985, pp. 483–500.

[84] Milnes, A. G., and D. L. Feucht, *Heterojunctions and Metal-Semiconductor junctions*, Academic Press, New York and London, 1972, pp. 34–93.

[85] Sze, S. M., *Physics of Semiconductor Devices*, 2nd edition, Wiley-Interscience, New York, 1981, pp. 480–486.

[86] Hurley, P. K., S. Taylor, W. Eccleston, and D. Meakin, "Determination of generation lifetime in intrinsic polycrystalline silicon," *Appl. Phys. Lett.*, *Vol. 54*, No. 16, 1989, pp. 1525–1527.

[87] Matsuura, H., S. Nishino, and H. Matsunami, "Fundamental properties of MIS solar cells using Mg-*p* Si system," *Jpn. J. Appl. Phys.*, *Vol 20*, Supplement 20-2, 1981, pp. 51–55.

[88] Matsuura, H., "Hydrogenated amorphous silicon/crystalline silicon heterojunctions: properties and applications," *IEEE Trans. Electron Devices*, *Vol. 36*, No. 12, 1989, pp. 2908–2914.

SYMBOLS

Symbol	*Unit*	*Description*
A	1/V	A constant of the junction-limited current for a-Si:H
B	At	A constant of the current flow from *p*-c-Si to a-Si:H
C	pF/cm^2	Capacitance of the heterojunction
C_2	pF/cm^2	Saturated capacitance at higher forward bias of a-Si:H
d_s	cm	Diode thickness
dV/dt	V/s	Voltage sweep rate
$D(E, t)$	eV	Function which takes a maximum at $[e_n(E) + e_p(E)]t = 1$
δ_1	eV	$E_F - E_V$ at *p*-c-Si
δ_2	eV	$E_C - E_F$ at a-Si:H
E_F	eV	Fermi energy (level)
E_F^a	eV	Fermi level at the neutral region of a-Si:H
E_{F_n}	eV	Quasi-Fermi energy of electrons
E_{F_p}	eV	Quasi-Fermi energy of holes
E_{g1}	eV	Energy bandgap of c-Si
E_{g2}	eV	Energy bandgap of a-Si:H
E_{OB}	eV	Energy level for which the thermal emission rate for electrons equals that for holes

Symbol	*Unit*	*Description*
E_{OB}^a	eV	E_{OB} in the neutral region of a-Si:H
E_p	eV	Energy level of the maximum value of $g(E)$
E_W	eV	Half width of the distribution
E_I	V/cm	Electric field
E_m	eV	Energy at which $D(E, t)$ takes a maximum value
E_C	eV	Conduction band edge
ΔE_C	eV	Conduction-band discontinuity
E_V	eV	Valence band edge
ΔE_V	eV	Valence-band discontinuity
$e_n(E)$	1/t	Thermal emission rate of electrons
$e_p(E)$	1/t	Thermal emission rate of holes
ϵ_{s1}	pF/cm	Semiconductor permittivity for c-Si
ϵ_{s2}	pF/cm	Semiconductor permittivity for a-Si:H
$f(E)$		Occupation function at $t = 0$ (Fermi-Dirac distribution function)
$F_\infty(E)$		Occupation functions at $t = \infty$
$g(E)$	1/cm^3/eV	Density-of-state distribution in a-Si:H
g_{max}	1/cm^3/eV	Maximum value of $g(E)$ of the Gaussian distribution
$H(t)$	1/cm^3	Transient HMC (heterojunction-monitored capacitance) signal
I	A	Current
I_0	A	Reverse saturation current
k	eV/K	Boltzmann constant
L	cm	Thickness of a-Si:H
N_A	1/cm^3	Density of shallow acceptors in *p*-c-Si
N_C	1/cm^3	Effective density of states in conduction band
N_t	1/cm^3	Density of midgap states between E_F^a and E_{OB}^a in a-Si:H
$^*N_t$	1/cm^3	Midgap-state density graphically estimated in the HMC method
$N_t(t)$	1/cm^3	Density of space charge at time t
$\Delta N_t(t)$	1/cm^3	Change in the space-charge density at time t
$N_t(\infty)$	1/cm^3	Density of space charge at time $t = \infty$
N_s	1/cm^3	Bulk spin density from electron spin resonance

Symbol	*Unit*	*Description*
N_{ss}	1/cm^3	Density of interface defects between *p*-c-Si and a-Si:H
n	1/cm^3	Electron density in the conduction band of a-Si:H
ν_n	1/tt	Preexponential factor of thermal-emission rates (attempt-to-escape frequencies) for electrons
ν_p	1/t	Preexponential factor of thermal-emission rates (attempt-to-escape frequencies) for holes
Q_I	C/cm^2	Space charge in region I ($W_{OB} < x \leq W_2$) in a-Si:H
Q_{ss}	C/cm^2	Space charge in the interface layer
ρ	1/cm^3	Space-charge density
S	cm^2	Electrode area
σ_2	1/Ωcm	Dark conductivity of a-Si:H
σ_n	cm^2	Capture-cross section of electrons
T	K	Absolute temperature
$u(x)$	eV	Potential energy
$u(x)$	eV	Potential energy shown in Figure 2(b)
u_{OB}	eV	Potential energy at W_{OB}
v_{th}	cm/s	Thermal velocity
V_B	V	Built-in voltage at the heterojunction
$^*V_B$	V	Built-in voltage graphically estimated in the HMC method
$V_C(t)$	V	Voltage at time t across the depletion region of c-Si
W_1	cm	Width of the depletion region of c-Si
W_2	cm	Width of the depletion region in a-Si:H
$W_1(t)$	cm	Depletion width in c-Si at time t
W_{OB}	cm	Cross point at $E_{Fn} = E_{OB}$ in a-Si:H

ACRONYMS

C-V	Capacitance-voltage
DLTS	Deep-level transient spectroscopy
ESR	Electron spin resonance
EV	Evaporated
GD	Glow discharge

GN	Gummel number
HBT	Heterojunction bipolar transistor
HMC	Heterojunction-monitored capacitance
I-V	Current-voltage
ICTS	Isothermal capacitance transient spectroscopy
MIS	Metal-thin insulator-semiconductor
MOS	Metal-oxide semiconductor
S/N	Signal-to-noise (ratio)
SB	Schottky barrier
SCLC	Space-charge-limited current
SIT	Silicon-intensifier target
SP	Sputtered

The Artech House Materials Science Library

Amorphous and Microcrystalline Semiconductor Devices, Volume I: Optoelectronic Devices, Jerzy Kanicki, ed.

Amorphous and Microcrystalline Semiconductor Devices, Volume II: Materials and Device Physics, Jerzy Kanicki, ed.

Electrical and Magnetic Properties of Materials, Philippe Robert

High-Speed Digital IC Technologies, Marc Rocchi, ed.

Indium Phosphide and Related Materials: Processing, Technology, and Devices, Avishay Katz, ed.

Introduction to Semiconductor Device Yield Modeling, Albert V. Ferris-Prabhu

Materials Handbook for Hybrid Microelectronics, J.A. King, ed.

Microelectronic Reliability, Volume I: Reliability, Test, and Diagnostics, Edward B. Hakim, ed.

Microelectronic Reliability, Volume II: Integrity Assessment and Assurance, Emiliano Pollino, ed.

Modern GaAs Processing Techniques, Ralph Williams

Vacuum Mechatronics, Gerado Beni, Susan Hackwood, et al.

VLSI Metallization: Physics and Technologies, Krishna Shenai, ed.

Amorphous and Microcrystalline Semiconductor Devices Volume II

Materials and Device Physics

Jerzy Kanicki, Editor

Artech House
Boston • London